UNIVERSITAT POLITÈCNICA DE VALÈNCIA

_ TELECOM ESCUELA TÉCNICA VLC SUPERIOR DE INGENIERÍA DE TELECOMUNICACIÓN

PHASE-CHANGE NANOMATERIALS WITH NON-VOLATILE MEMORY: CHARACTERIZATION AND ON-CHIP WIRELESS APPLICATIONS

Alejandro López Reche

Tutor: Javier Martí Sendra

Tutor Externo: Carlos García Meca

Trabajo Fin de Grado presentado en la Escuela Técnica Superior de Ingeniería de Telecomunicación de la Universitat Politècnica de València, para la obtención del Título de Graduado en Ingeniería de Tecnologías y Servicios de Telecomunicación

Academic Year 2020-21

Valencia, 4^{th} July 2021

Abstract

The objective of the Bachelor Thesis (BT) is the study of phase-change nanomaterials with non-volatile memory and the design of new integrable components in photonic integrated circuits (PICs) using these materials. In this work, phase-change materials based on $Ge_iSb_jTe_k$ (GST) compounds will be studied, as well as their use in CMOS-compatible photonics technology. In a first phase, the optical properties of GST nanolayers manufactured at the Nanophotonic Technology Center (NTC) will be experimentally characterized. Subsequently, the design and simulation process of a 3D wireless switching component will be carried out based on the use of a grating structure and its capability to radiate out of the plane that contains it. The development of these devices is of great interest for telecommunications applications (reconfigurable PICs, compact switching networks, high-capacity processing centers, new network typologies and technologies), as well as for other fields such as medicine, industry, military applications, photonic computing, and also allowing the creation of *Lab-on-a-chip* device of reduced dimension.

Key words:

Photonic devices, Photonic integrated devices, Phase-change materials with non-volatile memory, Wireless communications on-chip, reconfigurable photonic chips , 3D photonic devices, nanomaterials, nanoantennas

Resumen

El objetivo del Trabajo de Fin de Grado (TFG) es el estudio de nanomateriales de cambio de fase con memoria no volátil y el diseño de nuevos componentes integrables en circuitos fotónicos integrados (PICs) empleando dichos materiales. En este trabajo, se estudiarán materiales de cambio de fase basados en compuestos $Ge_iSb_jTe_k$ (GST), así como su uso en la tecnología fotonica CMOS-compatible. En una primera fase, se caracterizarán experimentalmente las propiedades ópticas de nanocapas de GST fabricadas en el Centro de Tecnología Nanofotónica (NTC). Posteriormente, se llevará a cabo el proceso de diseño y simulación de un componente de conmutación inalámbrica 3D basado en el uso del grating y su capacidad de radiar fuera del plano que lo contiene. El desarrollo de estos dispositivos resulta de gran interés para aplicaciones en telecomunicaciones (PICs reconfigurables, redes de conmutación compactas, centros de gran capacidad de procesado, nuevas tipologías y tecnologías de red), así como también para otros campos como la medicina, industria, aplicaciones militares, computación fotónica, y también permitiendo la creación de dispositivo *Lab-on-a-chip* de reducida dimensión.

Palabras clave:

Dispositivos fotónicos, Dispositivos fotónicos integrados, Materiales de cambio de fase con memoria no volátil, Comunicaciones inalambricas en chip, Chips fotónicos reconfigurables, Dispositivos fotónicos 3D, Nanomateriales, Nanoantenas

Resum

L'objectiu del Treball de Fi de Grau (TFG) és l'estudi de nanomaterials de canvi de fase amb memòria no volàtil i el disseny de nous components integrables en circuits fotònics integrats (PICs) emprant aquests materials. En aquest treball, s'estudiaran materials de canvi de fase basats en compostos $Ge_iSb_jTe_k$ (GST), així com el seu ús en la tecnologia fotònica CMOS-compatible. En una primera fase, es caracteritzaran experimentalment les propietats òptiques de nanocapes de GST fabricades en el Centre de Tecnologia Nanofotònica (NTC). Posteriorment, es durà a terme el procés de disseny i simulació d'un component de commutació *wireless* 3D basat en l'ús del grating i la seua capacitat de radiar fora del pla on es contingut. El desenvolupament d'aquests dispositius resulta de gran interés per a aplicacions en telecomunicacions (PICs reconfigurables, xarxes de commutació compactes, centres de gran capacitat de processament, noves tipologies i tecnologies de xarxa), així com també per a altres camps com la medicina, indústria, aplicacions militars, computació fotònica, i també permetent la creació de dispositiu *Lab-on-a-chip* de reduïda dimensió.

Palabras clave:

Dispositius fotònics, Dispositius fotònics integrats, Materials de canvi de fase amb memòria no volàtil, Comunicacions inalambriques en xip, Xips fotònics reconfigurables, Dispositius fotònics 3D, Nanomaterials, Nanoantenes

Contents

List of Figures

II GST Study

III GST Application

List of Tables

II GST Study

III GST Application

Part I

Introduction

Chapter 1

Introduction

1.1 Objective

The objective of this thesis is to understand the path to follow when developing a new technology or product. In this case the goal is to understand the underlying knowledge in phase-change materials and antenna theory to design a photonic device: a 3D wireless switch. The milestones for the project are summarized below:

- Define a framework for the different fields used in the design.
- Measure and acquire data from the phase-change materials and optically characterize them.
- Study the simulation process in antenna design.
- Design a working device for 3D wireless switching.

1.2 Methodology

To achieve the final goal of the project, the path to follow will be divided in several blocks stated below:

- Research of the state-of-the-art (SoTA) related to phase-change materials, nanoantennas, photonic integrated circuits and switches and set a framework to work with.

- Develop an understanding of the equipment used in the laboratories to measure and extract data from the materials. The equipment used was the Fourier-Transform Infrared Spectrometer.
- Simulate and extract the parameters of a working nanoantenna in CST Microwave Studio.
- Design and optimize a vertical wireless switch according to the specifications needed for its application.

1.3 Outline

This section is a general guide of the memory. It summarizes the content in each part and chapter to ease the understanding of the process and search of information. The project is divided in two main sections Part II and Part III introduced by Part I.

In Part II we describe the theoretical approach of the project, where the optical properties of the nanomaterial are studied and their actual values are experimentally retrieved.

In Part III we describe the theoretical basis of antennas, switches and the technology used for the final design. Subsequently, we depict the methodology we use to design and optimize the chosen structure.

In Part IV we present the results of the work and the final values obtained. Secondly, we conclude with the project and to close up we present the future work over the thesis.

Both II and III parts are divided into a theoretical/introductory section where the bases are stated and an experimental section where the student works on the information and data collected to elaborate on them.

Chapter 2

Organization: DAS Photonics

2.1 Description of the company

DAS Photonics S.L. was founded in 2005 as a spin-off of the NTC technological institute that focuses in the development of photonic technology and innovative products to meet the needs of different industries such us: defence, security, aeronautics, avionics, satellites and space.

2.1.1 Vision

The vision of the company is to provide high-end solutions based on photonics technology optimizing bandwidth, size, weight and power consumption.

2.1.2 Mission

The mission of DAS is to take up an international lead in the development of innovative products with high added value and specialization, based on technology with photonic properties that covers market needs of DAS strategic sectors.

2.2 Photonic devices

On its beginnings DAS was founded to develop photonics systems (modulators switches, filters and other passive systems) for space application and its business model grew towards new product lines such us electronics and defense.

Nowadays, DAS is specialized in photonic components for space and electronic devices for defense. Both powered by innovation, development, research and creativity. DAS stands up for new disrupting technologies and future generation devices, aiming for faster transmission rates, wider bandwidths, lower weight and volume and minimal power consumption.

Part II

GST Study

Index Retrieval

Chapter 1

Technological Foundation

1.1 Introduction to PICs

Photonics is essentially the science around generating a photon, its detection, manipulation, transmission, emission, signal processing, modulation, switching, amplification and sensing. Most photonics applications cover from near-infrared light (NIR) to visible light, although it could cover the entire electromagnetic spectrum [1].

The integration of photonics in a circuit is known as Photonic Integrated Circuits (PICs). As electronic integrated circuits, PICs interconnect several functionalities. By using the photon instead of the electron, integrated photonics is able to leverage higher frequencies, reaching the terahertz region, increasing the available bandwidth. This translates into an increment of the quantity of data which can be transported and handled. Its well-studied counterpart, electronics, cannot harness the high frequencies since communications based on electrical signals require conductors where waves travel through. As frequency rises, the impedance of the conductors follows along, therefore reducing the distance the wave can travel.

Moreover, electrical-based technology is limited by fundamental, material, device, circuit and system constraints [2]. These categories impact specific features such us implementation, validation, manufacturing, heat flow, cooling efficiency, interconnections or signal-to-noise ratios [3].

Photonic integrated circuits, by using photons instead of electrons, can use non-conductive materials as *"data highways"* where high frequency waves perceive the media as transparent and

low-loss (wavelengths around $1.3 - 1.6\mu m$).

The successful development (over the last >40 years) and commercialization (over the last >20 years) of PICs have been the result of numerous advances in materials processing and device capability. These and other advances over more than 50 years have enabled for InP PICS to integrate all required functions for transmitters/receivers reaching a scale of hundreds of elements per chip. As a result, this technology has been widely implemented for optical communications [4].

1.1.1 SiPICs and CMOS compatible PICs

The exponential trend of data transmission depicts an intrinsic shift in this era. The huge amount of devices interconnected rely on the revolution of communications, where the need of massive computation and scaling capabilities boosts the innovation.

Classical computation, where the core component is the electronic chip , is reaching its unavoidable physical limit in terms of size. Electronic and photonic integration has been envisioned as promising solution to the interconnect on-chip limitation [5]. The idea of bringing high-speed optical signals directly to a complementary metal-oxide-semiconductor (CMOS) chip offers opportunities for using light to aid electrical functions [6]. The silicon on insulator (SOI) has become the foundation of silicon photonics for its low cost, CMOS technology compatibility and strong optical confinement over wavelengths (λ) around 1550nm [7].

An electronic-photonic integrated circuit (EPIC) on silicon requires waveguides, lasers and photodetectors to receive, process and emit signals. Despite the high performance of InP based photodetectors, they are difficult to integrate with Si-based electronics. Consistent Ge-based photonics has been perceived as one of the most promising options to realize optical functionalities in Si CMOS-compatible SOI photonic circuitry [8]. Therefore, SiPICs and CMOS compatible PICs harness the silicon integrated circuits available technology (Figure 1.1) improved by the aid of photonics.

1.2 Introduction to PCMs

Phase-change materials (PCM) are a special group of semiconductors that alter their optical,

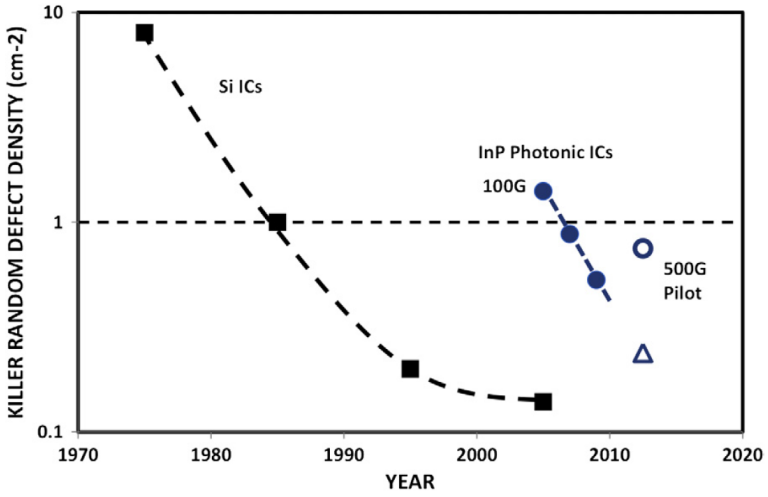

Figure 1.1: Killer random defect density [4]

Trends for killer random defect reduction versus time for Si ICs and InP large scale transmitter PICs for both 100-Gb/s transmitter products (solid circles) and 500-Gb/s transmitter (open circle) and receiver (open triangle) products. The 100-Gb/s data points represent average production performance whereas the 500-Gb/s data points are based on sampling of better performing wafers during early production.

dielectric, and electrical properties by changing its solid state internal configuration. This phase transition is due to a reversible transformation achieved by optical or thermal stimuli [9]. Current optical PCM such us $G_iS_jT_k$ present a significant change on its refractive index Δn and optical loss (Δk), simultaneously. This increment in both optical properties constraints the scope of the applications for which PCM can be used [10].

The phase change experienced by the materials is caused by an atomic lattice reconfiguration from an amorphous to a crystalline phase and vice versa (Figure 1.2). The PCM reaches its crystallization temperature and almost-free atoms begin the crystal nucleations and growth process. The crystallization set time is of the order of tens of nanoseconds. However, it depends on the exact material configuration. The material crystallizes into a geometrical-like mesh acquiring low resistance and high reflectivity. This process is called setting.

The reverse phase change is called resetting and requires a high temperature to melt the compound and release all the molecular bounds of the internal structure. By rapidly quenching the liquid state, the PCM does not crystallize and reach the amorphous phase. The temperature needed to melt the PCM is of the order of hundreds of ºK and the resetting time requires a rapid cooling. Therefore the resetting process is finished over tens of picoseconds (Figure 1.3b).

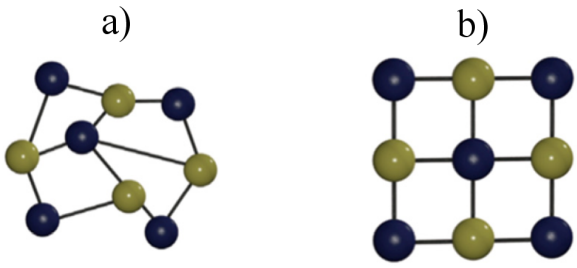

Figure 1.2: PCM phases

a) Amorphous b) Crystalline

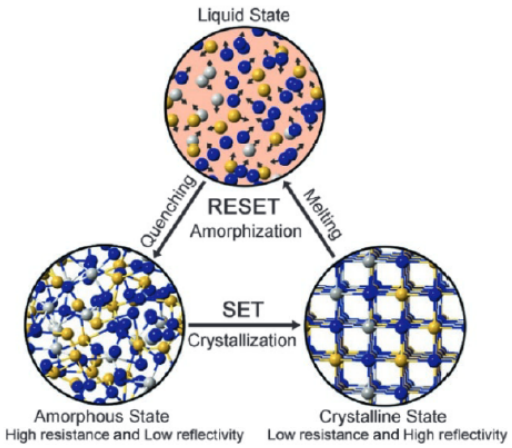

(a) PCM states

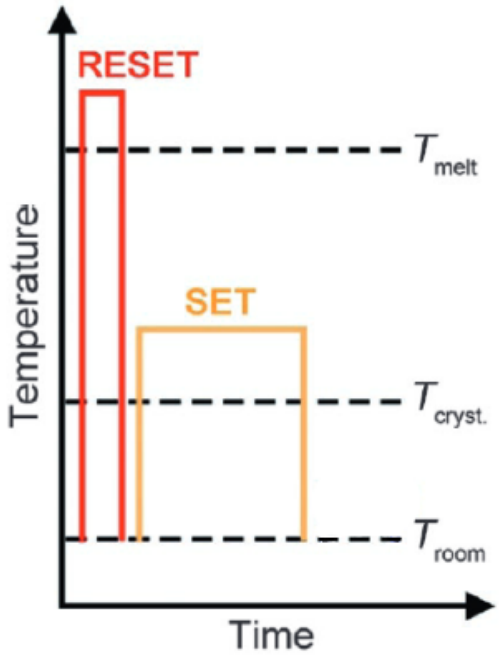

(b) Phase-change specifications

Figure 1.3: PCM phase change [11]

Since the phase change requires a relative high temperature for both phase switches, the phase conservation is non-volatile at room temperature and can last as long as the material lasts. Research has also shown the capability of intermediate phases [12]. The multi-level phases characteristics lead to the possibility of generating all-photonic memories that leverages the non-volatile nature of the compound.

1.2.1 GST

In this thesis we will work upon some GST compounds (Figure 1.4), as it is one of the most studied PCMs together with VO_2 (although the latter has a volatile memory). GST amorphous phase is an optical transmissive, electrically resistive state where GST crystalline state present opaque optical properties and conductive electrical responsivity [13] for 3^{rd} window of telecommunication (this could not be the case at all frequencies as, for example, GST_c is optically transparent for $3.3\mu m$). GST melting point is achieved at temperatures around 850ºK and its crystallization temperature around 450ºK.

PCM characterization plays a main role when using these compounds in a design. It is widely known that the optical properties of PCMs show a large variability, as they depend on the PCM exact molecular configuration (Figure 1.5).Because of this issue, we approach this limitation by providing a methodology to conduct its optical characterization, as it is crucial when using PCMs.

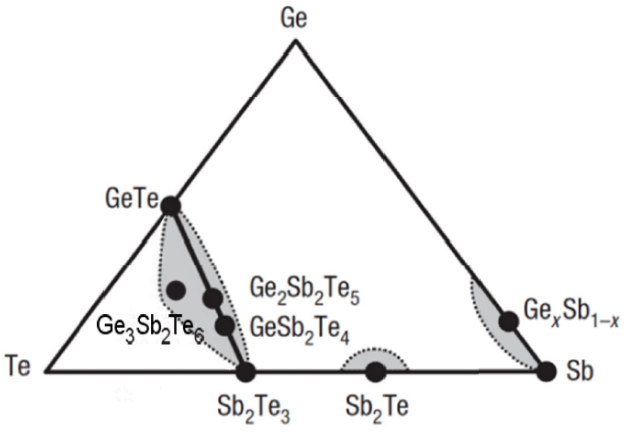

Figure 1.4: GST triangular compound graph

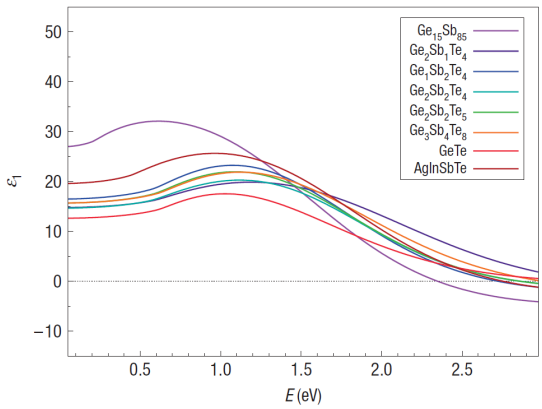

(a) Amorphous state ε_1

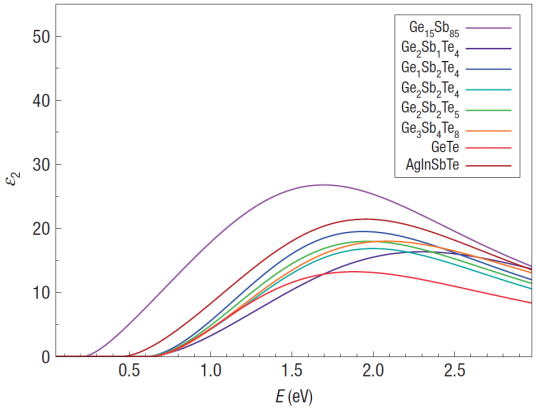

(b) Amorphous state ε_2

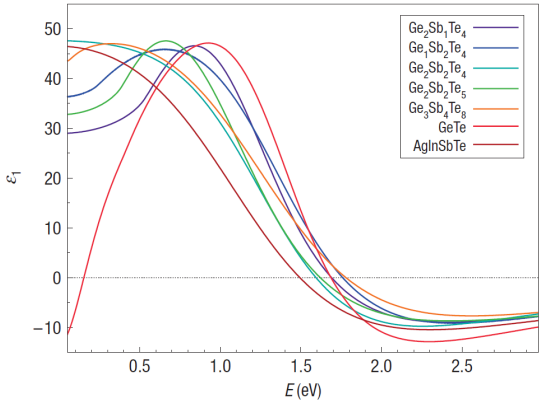

(c) Crystalline state ε_1

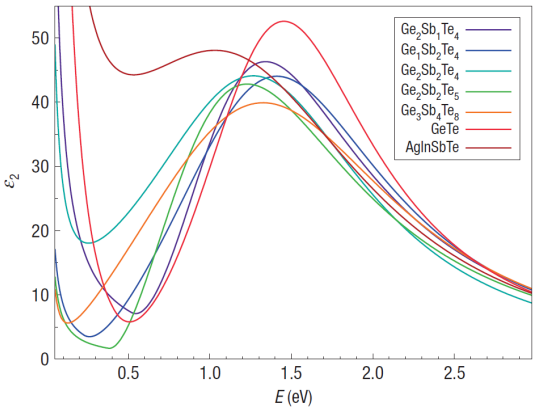

(d) Crystalline state ε_2

Figure 1.5: GST phases optical characteristics[14]

Chapter 2

Refractive Index Retrieval

This part focuses on developing an understanding of the different blocks used in the index retrieval. The algorithm relies on both, experimental and numerical methods. The experimental measurements are based on [14] retrieving the refractive index from ellipsometry and FTIR Spectrometer data. The numerical method harnesses the well-known powerful tool TMM (Transfer Matrix Method) to calculate the reflections in a thin layered structure with specific refractive index over frequency (f). For this section we will use Tauc-Lorenz model with an added Drude contribution (TLD).

2.1 Methodology and materials

Firstly, we decide the equipment used for the measurements. In [14], they use the FTIR in reflection and spectroscopic ellipsometry. Since the spectral range needed for the study includes both 3^{rd} telecommunications window and wavelength (λ) $= 3.3\mu m$ (this will be discussed in 2.1.1) we conclude that FTIR will be used in the measurements as NTC ellipsometer does not accept the upper wavelength.

Secondly, it must be said that the measurements obtained from the FTIR are absolute magnitudes as it gathers the reflected energy from the sample as a percentage of the source beam. Consequently, there is a limitation when extracting the index considering both real and imaginary values, as the two degrees of freedom cannot be resolved with a data-set. This drawback is diminished by extracting another measurement (transmission magnitude, transmission phase or reflected phase).

As phase measurements are hard to deal with in the optical regime and reflection calculations are simpler with an ideal-like mirror as a substrate (Gold is almost an ideal mirror in the optical range taken into consideration) we base on a data-set algorithm constraining the inherit freedom of the measurements by adapting the refractive index to an accurate physical model, the TLD model.

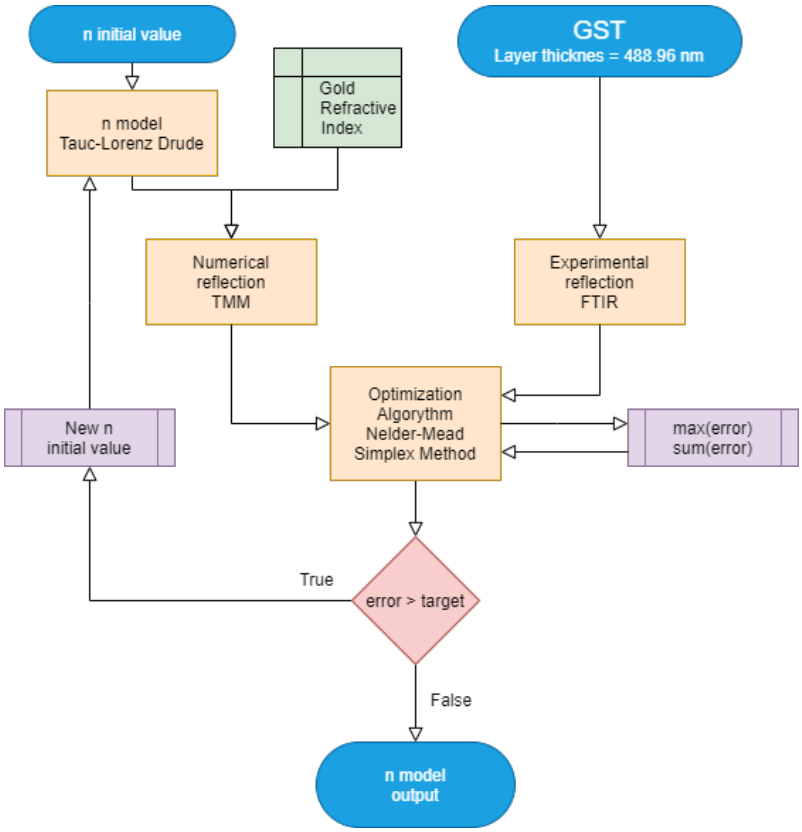

Figure 2.1: Index retrieval algorithm

2.1.1 GST 225 & 326

GST_{225} and GST_{326} will be the main materials studied in the thesis. Both materials are chosen because they present a high resolution phase change at the 3^{rd} telecommunication window without acquiring significant losses and could be used in other applications in $\lambda = 3.3\mu m$ due to its absolute minimum losses. These two conditions provide sufficient usability in photonic integrated circuits among other applications.

2.1.2 FTIR Spectroscopy

For the extraction of the data, a Fourier Transform Infrared Spectroscopy (FTIR) analysis is used. An FTIR spectrometer allows the transmission or absorption spectrum to be obtained from a specific sample. In order to do so, the FTIR software uses the Fourier Transform mathematical process to translate the raw data received from the sensor to obtain the infrared spectrum of the material. This mathematical process is used over the data received at the detector which has been interfered with itself by using a beamsplitter and a couple of mirrors (one fixed and the other moving). With this counterintuitive way of measuring the reflected or absorbed signal output of a sample, it is possible to get broadband measurements in short time spans (compared to dispersive monochromatic spectroscopy).

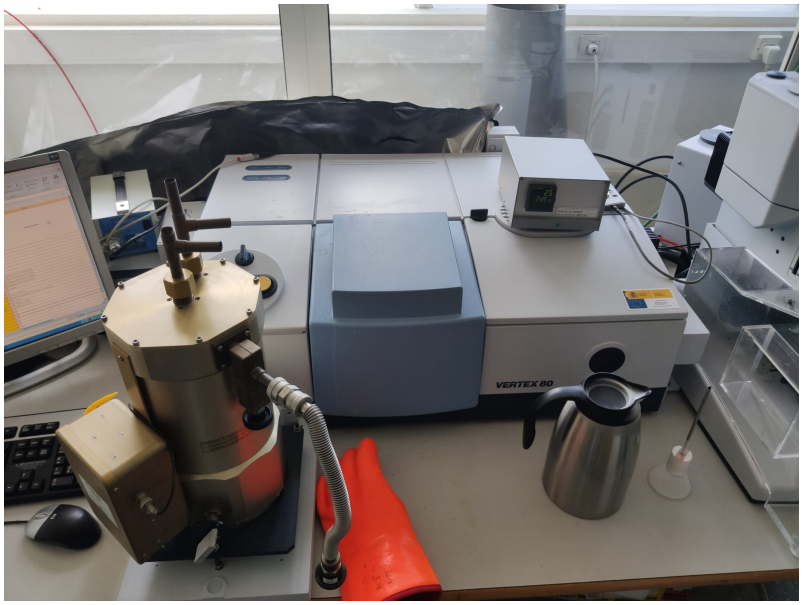

Figure 2.2: FTIR used for the measurements

The FTIR spectrometer used in this project allows us to measure optical reflection and transmission in a wavenumber (ν) range from $40.000cm^{-1}$ to ν= $4cm^{-1}$. Since the spectral region of some of the most interesting photonic applications of GST includes the 3^{rd} telecommunications window (λ = 1550 nm or f = 193.616 THz) and the mid-infrared band around $\lambda = 3.3\mu m$, the measurements cover both ν= $6456cm^{-1}$ and ν= $3000cm^{-1}$ respectively.

While measuring, the beam which radiates the sample also goes through several devices. Due to this, the bandwidth where the measurement takes place is constrained by the combined spectral

response of the different elements of the equipment. The basic limiting elements are the beam splitter, the laser source and the detector (see Figure 2.3.). According to the equipment specifications (Annex A attached), this forces us to use two different FTIR configurations to cover the spectral band of interest (see Table 2.1).

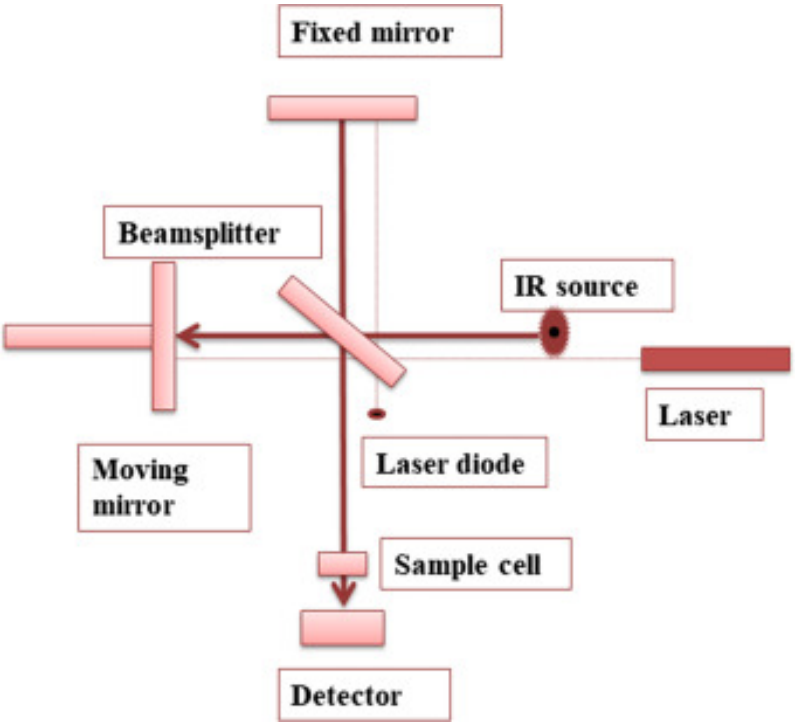

Figure 2.3: FTIR Schematic diagram [15]

By checking the working bandwidth where the equipment works (Annex A attached) selecting the devices used for the measurements is straightforward, leaving a setup such us Table 2.1.

	Laser	Beamsplitter	Detector
$10.000 - 5.000 cm^{-1}$	Tungsten	T401 CaF_2 VIS/NIR	MCT D316
$5.000 - 500 cm^{-1}$	Globar	T303 KBr	MCT D316

Table 2.1: FTIR Equipment used

Given that the PCM sample has to be externally heated while measuring, so its optical prop-

erties can be studied while changing its state, a hot plate is used to raise the sample temperature from room temperature to 180ºC. Due to the use of a bulk device such us the heater, a microscope has to be used in the setup to focus the beam onto the sample outside of the FTIR spectrometer to obtain the reflected energy (Figure 2.4)

(a) Microscope linked to the setup **(b) Sample heating plate**

Figure 2.4: FTIR Extra equipment

2.1.3 Measurements

The student had the opportunity to participate in the final measurements, which were carried out under the guidance of Miroslavna Kovylina at the NTC laboratories (8F, Camino de Vera, 46022 Valencia). The data was segmented in two ranges ($10.000 to 5.000 cm^{-1}$ and $5.000 to 500 cm^{-1}$) containing each of them a required ν($6456 cm^{-1}$ and ν= $3000 cm^{-1}$ respectively).

2.2 Index retrieval

In this section, we develop the index retrieval methodology and building blocks of the implemented algorithm (Figure 2.1). Subsequently, we discuss over the result and the interpretation of the data obtained.

2.2.1 Retrieval algorithm

The aim here is to extract the optical characteristics from the extracted raw data. Therefore, we implement a Matlab script where an algorithm runs and processes FTIR output data. Since the data retrieved represents the reflections of the input beam inside the sample, a mathematical method is needed to calculate the interaction of the light while it propagates through a multilayer stack of materials (see Figure 2.5).

A challenging problem which arises from this domain, is the degrees of freedom available in the structure. Only the reflected amplitude of the system is measured since the sample under study is constructed over a gold substrate (mirror like material within the frequency range) and it leads to a multiple-solution problem. One approach to solve this problem involves the use of a model so the increased degrees of freedom are constrained.

Lastly, both methods are used in the script to determine the model variables which define the material by minimizing the error found when applying a Nelder-Mead Simplex Method [16], already implemented in Matlab. The results are compared with the literature and represented below (Section 2.2.4)

2.2.2 The Transfer Matrix Method

The transfer matrix method (TMM) is the one of the most powerful methods of contemporary theoretical physics. By leveraging the conservation of the field's tangential component, it is possible to generate a connection of the fields in each layer (Figure 2.5).

This method is also used to yield an accurate solution for the one-dimensional lattice-gas model, i.e., describing the thermal desorption spectra [18]. This technique can also be used very effectively to solve two-dimensional problems (Figure 2.6), for example to calculate phase diagrams

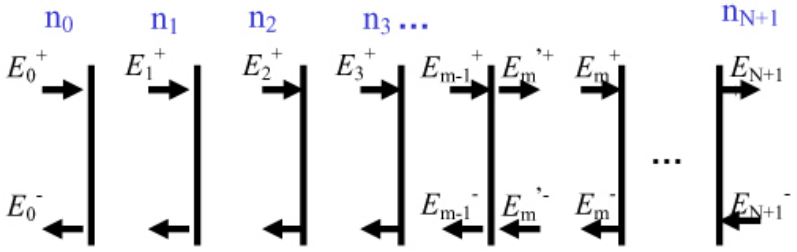

Figure 2.5: TMM 1D multilayer system [17]

of adsorbed overlayers [19]. Therefore, TMM is a fitting method for our problem: a multi-layer electromagnetic system.

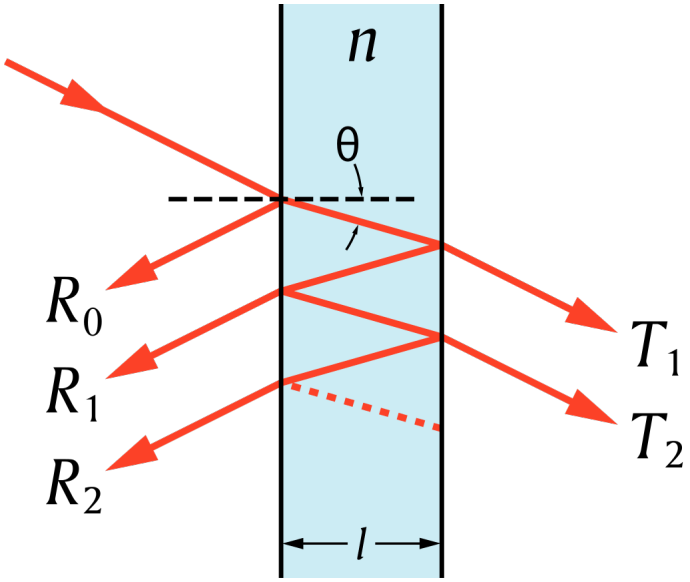

Figure 2.6: TMM 2D beam propagation [20]

Our structure consists of three different layers: air, GST and gold. First, we describe the characteristic matrix of a single layer M giving the following relation between the incident field and the last field transmitted [21][22]:

$$\begin{pmatrix} E_0 \\ H_0 \end{pmatrix} = M \begin{pmatrix} E(Au) \\ H(Au) \end{pmatrix} \tag{2.1}$$

Where E is the electrical tangential component of the electromagnetic field and H its magnetic tangential component. Since the structure has multiple layers where the beam interacts with the materials, in each layer the field will behave as if it was a single layer:

$$\begin{pmatrix} E_{j-1} \\ H_{j-1} \end{pmatrix} = M_j \begin{pmatrix} E_j \\ H_j \end{pmatrix} \tag{2.2}$$

Where M_j is a matrix that describes the interaction of the wave in a given media or layer:

$$M_j = \begin{pmatrix} cos(\phi_j) & \frac{isin(\phi_j)}{n_j} \\ i \cdot n_j \cdot sin(\phi_j) & cos(\phi_j) \end{pmatrix} \tag{2.3}$$

Where:

$$\phi_j = k_0 \cdot d_j \cdot n_j \tag{2.4}$$

Being $k_0 = \frac{c_0}{f} = \frac{2\pi}{\lambda}$, d_j the thickness and n_j the refractive index of the j^{th} layer respectively. The characteristic matrix of a multilayer corresponds to the multiple matrices M_j multiplied, and the relation becomes:

$$\begin{pmatrix} E_0 \\ H_0 \end{pmatrix} = \prod_{j=1}^{m-1} M_j \begin{pmatrix} E(Au) \\ H(Au) \end{pmatrix} = M_t \begin{pmatrix} E(Au) \\ H(Au) \end{pmatrix} \tag{2.5}$$

To put it in another way, we call M_t to the product of all M_j matrices, and by Equation 2.1 we get that $M_t = M$ being M the characteristic matrix of the multilayer. To conclude M is constructed as:

$$M = \begin{pmatrix} M_{11} & M_{12} \\ M_{21} & M_{22} \end{pmatrix} \tag{2.6}$$

Lastly, the resulting expressions of the amplitude of reflection (r) and transmission (t) are:

$$r = \frac{n_o \cdot M_{11} + n_0 \cdot n_{Au} \cdot M_{12} + M_{21} - n_{Au} \cdot M_{M22}}{n_o \cdot M_{11} + n_0 \cdot n_{Au} \cdot M_{12} + M_{21} + n_{Au} \cdot M_{M22}} \tag{2.7}$$

$$t = \frac{2n_0}{n_o \cdot M_{11} + n_0 \cdot n_{Au} \cdot M_{12} + M_{21} + n_{Au} \cdot M_{M22}} \tag{2.8}$$

The energy coefficients of reflectivity and transmissivity are given by:

$$R = |r|^2 \tag{2.9}$$

$$T = \frac{n_{Au}}{n_0}|t|^2 \tag{2.10}$$

With this mathematical method, we are able to calculate the response of a set of refractive indexes in a certain multilayer structure.

2.2.3 Tauc-Lorenz Drude model

As it has already been discussed, a physical reliable model is used to constrain the freedom inherited from the simplification of the measurements. The model used for this purpose is the Tauc-Lorenz (TL) with a Drude contribution. The full development of the equation is found in [23], as well as the specifications of the values in the model.

$$\varepsilon(\omega) = \varepsilon_{\text{const}} + \varepsilon_{\text{Drude}}(\omega) + \varepsilon_{\text{TL}}(\omega) \tag{2.11}$$

$$\varepsilon_{\text{Drude}}(\omega) = \frac{\omega_p^2}{\omega(\omega + i\gamma)} \tag{2.12}$$

$$\varepsilon_{TL} = \varepsilon_{r,TL} + i \cdot \varepsilon_{i,TL} = \varepsilon_{r,TL} + i \cdot (\varepsilon_{i,T} \times \varepsilon_{i,L}) \tag{2.13}$$

$$\varepsilon_{i,T}(E > E_g) = A_T \cdot \left(\frac{E - E_g}{E}\right)^2 \tag{2.14}$$

$$\varepsilon_{i,L}(E) = \frac{A_L \cdot E_0 \cdot C \cdot E}{(E^2 - E_0^2)^2 + C^2 \cdot E^2} \tag{2.15}$$

$$\varepsilon_{r,TL}(E) = \varepsilon_r(\infty) + \frac{2}{\pi} \cdot P \cdot \int_{E_g}^{\infty} \frac{\xi \cdot \varepsilon_i(\xi)}{\xi^2 - E^2} d\xi \tag{2.16}$$

$$\varepsilon_{i,TL}(E < E_g) = 0 \tag{2.17}$$

2.2.4 Methods

By comparing both TMM reflectivity and data measurements extracted from the FTIR spectroscopy, we first indicate if the material we are using is similar to the one present at the literature, as the production procedure could potentially modify the stoichiometry and homogeneous characteristic of the compound. This adds another layer of relevance in the study and simplification of optical characterization.

GST_{225} reflectance in the amorphous state presents a similar behaviour (Figure 2.7a). Although, the phase-change to crystalline (Figure 2.7b do not match the expected values as it appears to be compressed in the lower frequencies. GST_{326} behaviour matches the peaks at lower frequencies at both amorphous and crystalline (Figures 2.8a & 2.8b). However, in the amorphous phase it present a lower reflectivity than expected, potentially implying grater *n* and *k* at higher frequencies.

This versatility of optical characteristics is an issue when working with GST. The production procedures and other variability in the purity of the sample (Figure 1.4) are the main key factors that give importance to the optical characterization of the samples we work with, and therefore, the implementation of a method to retrieve this information.

For starting the algorithm, two inputs are needed (see Figure 2.1): the gold optical characterization as the substrate and the initial values for the refractive index. The gold data set was taken from [24]. For the initial refractive index values input, we use values extracted from [23], as they prove to be a sufficiently close value to begin with.

2.3 Results

The optical characteristics of GST_{225} and GST_{326} match the objectives found in [14] and present the index increment ($\Delta\varepsilon$) from the amorphous to the crystalline phase.

As it was exposed before, the refractive index does not have to exactly match the literature. Nonetheless, we extracted significant values as the error in the reflectance approximation is minimal. This scenario is not followed by the crystalline phase in GST_{225} and error bound to emerge in the results.

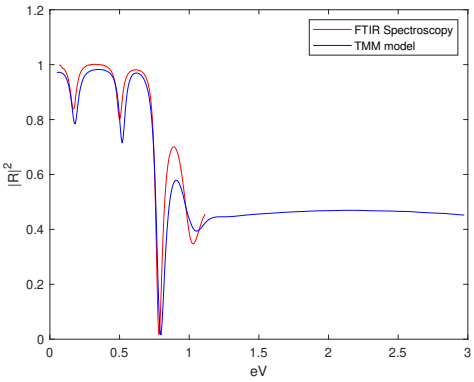

(a) Amorphous reflectivity comparison

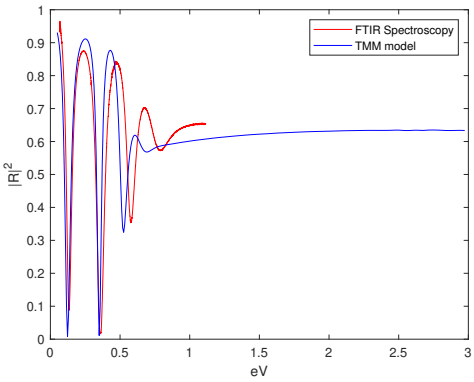

(b) Crystalline reflectivity comparison

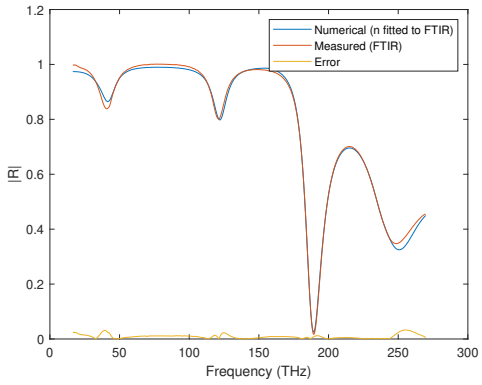

(c) Reflectivity amorphous phase

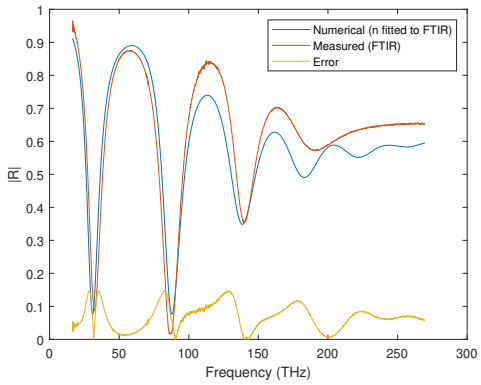

(d) Reflectivity crystalline phase

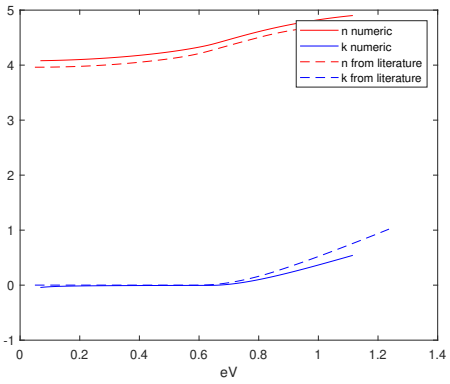

(e) Refractive index amorphous phase

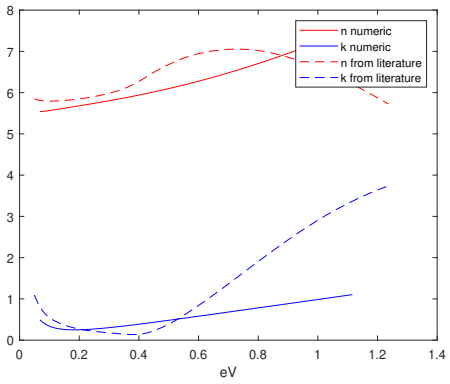

(f) Refractive index crystalline phase

Figure 2.7: GST_{225} **characteristics**

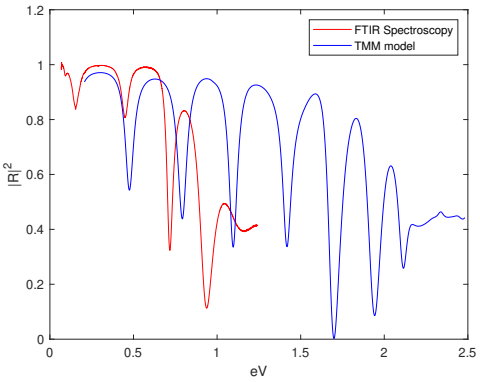

(a) Amorphous reflectivity comparison

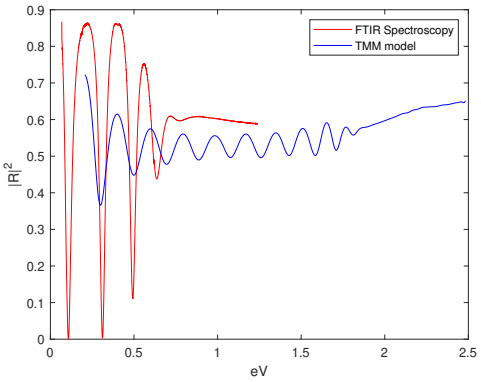

(b) Crystalline reflectivity comparison

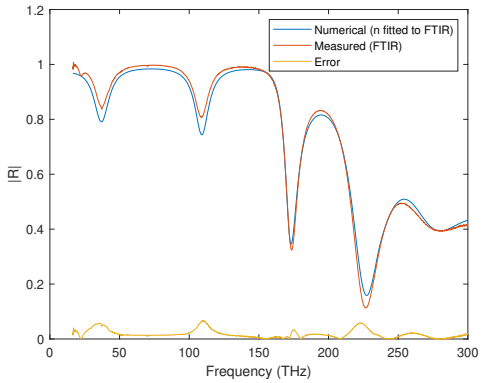

(c) Reflectivity amorphous phase

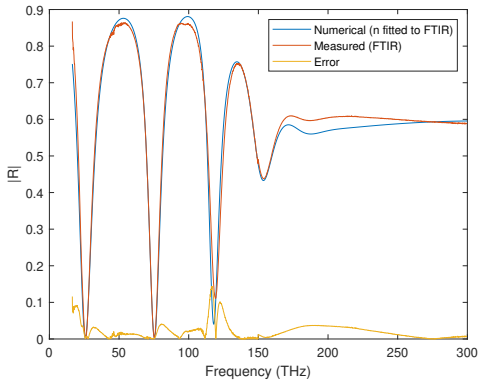

(d) Reflectivity crystalline phase

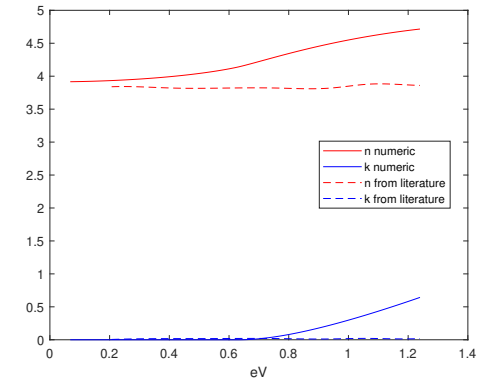

(e) Refractive index amorphous phase

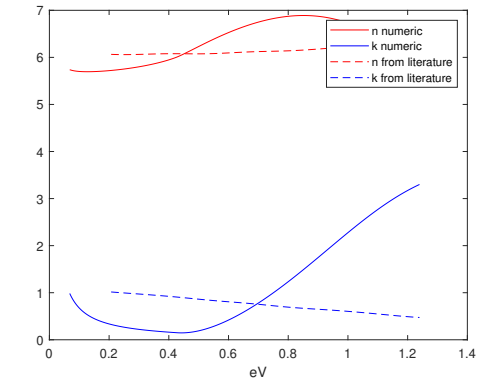

(f) Refractive index crystalline phase

Figure 2.8: GST_{326} **characteristics**

Finally, we present the Tauc-Lorentz Drude model parameters extracted with the algorithm in Table 2.2 for GST_{225} and in Table 2.3 for GST_{326} .

	E_g	ε_∞	A	E_0	C	w_p	w_c
Amorphous	0.6362	10.0554	192.7247	3.5078	7.0657	-662.9077	-1.2271e4
Crystalline	0.0822	-135.4429	575.4752	3.2098	0.8418	-1.9973e3	7.0523e3

Table 2.2: GST_{225} **parameters**

	E_g	ε_∞	A	E_0	C	w_p	w_c
Amorphous	0.6312	1.1649	101.4846	2.4793	2.6560	-7.1061e-4	0.0017
Crystalline	0.4286	8.9046	110.2831	1.2519	1.2519	-1.4619e-4	1.8281e5

Table 2.3: GST_{326} **parameters**

The model proves to be a keen tool to diminish the uncertainty of the measurements. This method provides a quick easy algorithm to characterize the optical behaviour of a material by analyzing its reflective spectra over a sample.

It was shown that different processes of GST nanofilms production do not display a unique refractive index profile. Therefore, making the optical characterization of the material is fundamental instead of relying on the values given by the literature.

Part III

GST Application

3D Wireless Switch

Chapter 1

Theoretical Foundation

1.1 Switching background

With current increasing necessities for data computation, a change towards server-side computation is being experienced. Client-side computing does not meet the specifications required for massive data processing in advanced applications in fields such as high performance computing (HPC), big data, deep learning and artificial intelligence (AI) or aerospace.

Server-side computation needs wide area warehouse-scale computer (WSC) or data centers to keep the different components (processors, memories, storage, interconnection networks and devices, cooling systems, power supplies, control units among others). Data centers are one of the most energy-intensive building types, consuming 10 to 50 times the energy per floor space of a typical commercial office building. Collectively, these spaces account for approximately 2% of the total USA electricity use [25]. It is not a surprise the energy-efficient requirement at these WSC and the efforts towards the optimal performance-per-Watt.

As it has already been said, photonics and photonic integration aid the already well-known electric devices used in data centers, providing a wide-band communication backbone, high data rate and low losses over long distances. During the last years, the use of optical switches has been widely spread to route signals among multiple sources and destinations in telecommunication and data centre networks. The integration of electronics and photonics and the implementation of new highly-complex multi-functional PICs are able to provide a solution to this issue.

Several types of optical switches have been broadly studied, such us:

- Mach-Zehnder interferometer (MZI) switches commonly consist of two 3 dB couplers and a dual-waveguide arm between them, one of them combined with a phase shifter to achieve the interferometric characteristics of the device. The principles behind the MZI provide broadband switching capabilities [26] (Figure 1.1a).

- Micro-ring resonators (MRR) are resonant structures that allow a selective wavelength filtering switching applications. Compared to the MZI switches, MRR switches are characterized for its smaller footprint (resonant capabilities rely on the wavelength comparable size of the component). This component allows the switch of a certain wavelength between two ports (red and blue arrows in Figure 1.1b).

- Liquid-crystal (LC) optical switches exploit the optical properties of these materials. Liquid crystals present an intermediate phase between solid and liquid state presenting some interesting mechanical properties of its molecular alignment. The molecular layout can be controlled by an electric field across the cell managing the manipulation of its refractive index and birefringence. With its characteristics it can be used in free space designs and allow the assembly of relative medium size switching matrices over planar waveguide structures.

- Micro-electro-mechanical systems (MEMS) are a key device in space optical switching by leveraging macroscopic opto-mecanical switching features, such us mirrors, shutters and lenses, adding the advantages of small size, speed and batch-fabrication. The classification of MEMS can be divided into two groups depending on the phenomena used to achieve the switching: reflective/refractive structures and difractive/interference structures [27].

- Silicon optical antennas [28] are nanostructures based on traditional antenna concepts which allow the manipulation and radiation of electromagnetic fields within a chip. Leveraging this concept we are able to switch seamlessly light emitters and receivers with a reduced crosstalk, simple fabrication and high performance. These features and characteristics favor silicon optical antennas to be used for our design over the other technologies.

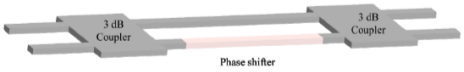

(a) MZI switch

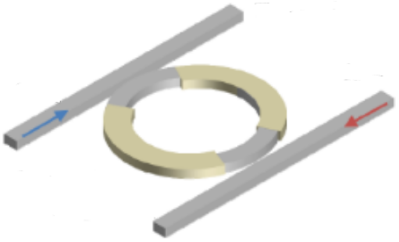

(b) MRR switch

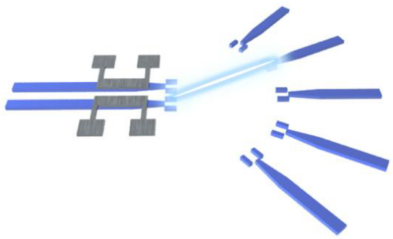

(c) Silicon optical antenna

Figure 1.1: Integrated optical switches [26, 28]

1.1.1 3D Interconnectivity

As it has already been discussed, the growth trend in computational needs and bandwidth requirements plays an angular research field in the incoming years. Current research is focused on developing and perfecting the so called Networks-on-a-chip (NoC). As the physical limitations reach its unavoidable end and the demands in data transfer and energy efficiency increases, NoCs traditional electrical architecture development is obstructed by the electronic bottleneck. Researches foresight the demands and new emerging technologies such as silicon photonics and 3D stacking are under consideration.

3D silicon integration in which multiple device layers are stacked on top of each other with direct vertical interconnects tunneling through them by using, for instance, through-silicon vias (TSV) or different kinds of vertical couplers [29, 30] promises to address many key challenges arising from the semiconductor industry. As size keeps shrinking, integration densities increase the hoops and delay between source and destination. By providing another dimension or layer, connection delays can substantially be reduced. High demanding bandwidth applications such us video or graphic processing could potentially benefit from this and avoid the latency penalty inherent of wider bandwidths. Finally, 3D interconnectivity eases the implementation of hybrid technologies at different levels like EPICs onto a single multi-layer design.

Whereas 3D stacking and its 3D interconnections keep on developing, photonics flexibility and versatility must meet these requirements. Current PIC devices rely on fixed layouts with guided interconnects limiting its reconfigurability and incrementing the complexity of their topologies [28]. Disruptive technologies such us Wireless Silicon Photonics and wireless nanostructures aim to overcome these limitations in the optical NoCs enabling us to dynamically reconfigure the interconnections of a PIC (Figure 1.1c). 3D wireless interconnects will definitely redraw the architectures in future WSC. Following all the previous ideas, the final objective of this thesis will be the development of an on-chip 3D wireless switch with a non-volatile memory, based on dielectric nanoantennas and GST nanostructures.

1.2 Antenna theory

In this section, some antenna parameters used throughout the thesis will be briefly defined. The following list of parameters are taken from the IEEE 145-2013 - IEEE Standard for Definitions of Terms for Antennas [31].

Directivity

The directivity D is defined as "The ratio of the radiation intensity (K) in a given direction from the antenna to the radiation intensity (K_0) averaged over all directions. The average radiation intensity is equal to the total power radiated (P_{RAD}) by the antenna divided by 4π." The mathematical expression of this definition is:

$$D(\theta,\phi) = \frac{K(\theta,\phi)}{K_0} = 4\pi\frac{K(\theta,\phi)}{P_{\text{RAD}}} \tag{1.1}$$

Where θ is the angle formed in between the *z* axis to the line connecting the origin to the point in a 3D space, and ϕ the angle formed from the *x* axis to the line connecting the origin to the point in a 3D space.

The maximum directivity is also expressed with the letter D. However, it is not specified the direction meaning that it is understood to be the direction of maximum radiation.

$$D = D(\theta,\phi)\Big|_{max} = \frac{K_{max}}{K_0} = 4\pi\frac{K_{max}}{P_{\text{RAD}}} \tag{1.2}$$

Therefore, the directivity measures the antenna distribution of radiated power. In this sense, high directivity antennas will radiate most power in a certain direction, and low directivity antennas emit the same power distributed over a wider angular range.

Radiation diagram

The radiation diagram is the mathematical expression that represents the radiation properties of an antenna. This diagram determines the far-field radiation of the antenna and it is commonly represented as a combination of two perpendicular 2D sections of itself called E and H section.

The radiation diagram's range of values goes from 0 to 1, since it only represents how much energy is radiated in each direction. It is described mathematically as:

$$d(\theta, \phi) = \frac{|E(\theta, \phi)|}{|E_{max}|} \tag{1.3}$$

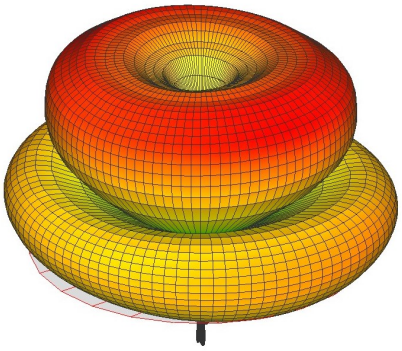

Figure 1.2: Example of radiation diagram [32]

Radiation efficiency

The radiation efficiency is defined as "The ratio of the total power radiated by an antenna to the net power accepted by the antenna from the connected transmitter". It describes the proportion of the power that the antenna radiates from an input accepted power. It can be expressed as:

$$\eta_{\text{RAD}} = \frac{P_{\text{RAD}}}{P_{\text{IN}}} \tag{1.4}$$

Total efficiency

The total efficiency is defined as "The ratio of the total power radiated by an antenna to the net power inserted to the antenna from the connected transmitter". It describes the proportion of the total power inserted from an input that the antenna radiates. It can be expressed as:

$$\eta_{\text{TOT}} = \frac{P_{\text{RAD}}}{P_{\text{TOT}}} \tag{1.5}$$

IEEE Gain

The IEEE gain of the antenna is one of the most used objectives when designing an antenna. It is defined as "The ratio of the radiation intensity in a given direction to the radiation intensity that would be produced if the power accepted by the antenna were isotropically radiated"

$$G_{\text{IEEE}}(\theta,\phi) = \frac{K(\theta,\phi)}{P_{\text{IN}}^{\text{ISO}}} = \eta_{\text{RAD}} \cdot D(\theta,\phi) \tag{1.6}$$

Realized Gain

The realized gain of the antenna is defined as "The ratio of the radiation intensity in a given direction to the radiation intensity that would be produced if the power fed by the antenna were isotropically radiated"

$$G_{\text{REALIZED}}(\theta,\phi) = \frac{K(\theta,\phi)}{P_{\text{TOT}}^{\text{ISO}}} = \eta_{\text{TOT}} \cdot D(\theta,\phi) \tag{1.7}$$

Chapter 2

Applications

The objective of the design is to elaborate a structure capable of 3D switching. We use GST as a switching mechanism due to its phase change refractive index difference. This attribute of PCM allow us to reconfigure the device at will with an extremely compact device. The optical stimuli is considered for this application as it allows to change the optical properties without a heating structure [12].

Different structures had been taken into consideration for the application. These previous ideas (Figure 2.1) relied on concepts such us: total reconfiguration of the antenna (Figure 2.1a), the destructive interference of the radiated fields (Figure 2.1b) or Yagi-Uda antennas (Figure 2.1c).

The best performance antenna was the Yagi-Uda approach. Further study of the structure showed the radiating phenomena was mainly from grating interference as there was no direct director being fed for the Yagi-Uda design. That is why we focused on developing a grating-like antenna to design the envisioned 3D wireless switch.

2.1 Antenna overview: Grating antenna

Gratings have been widely studied due to its particular interest to scientists and engineers, and it has contributed to modern physics due to its wide range of applications [33].The former head of Spectroscopy Lab and later Dean of Science at MIT, George R. Harrison (1898-1979) once wrote: "No single tool has contributed more to the progress of modern physics than the diffraction grating,

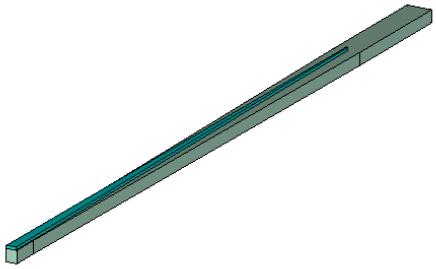

(a) Antenna reconfiguration

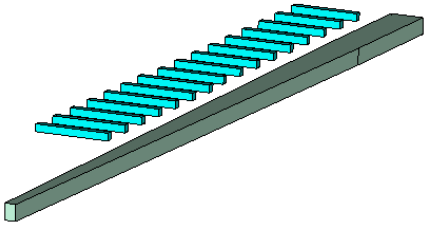

(b) Destructive interference

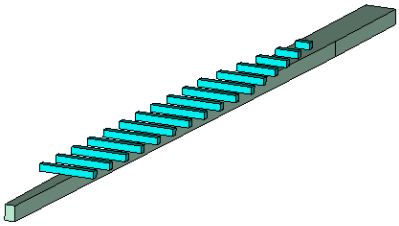

(c) Yagi-Uda

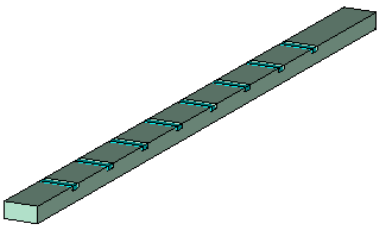

(d) Grating antenna

Figure 2.1: Designs taken into consideration

especially in its reflecting form [34]."

Conceptually, a grating is a simple periodic structure where its pattern interacts with incident electromagnetic waves, resulting in a physical phenomenon called diffraction which splits the beam into several directions (or orders) (Figure 2.2).

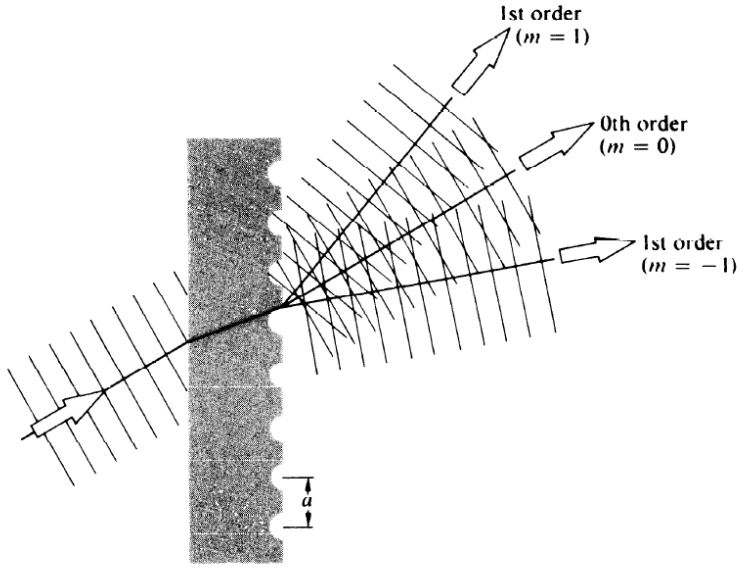

Figure 2.2: Transmission grating and orders of diffraction [35]

Gratings are widely used for their capabilities in a number of applications related to, for example, wavelength-selective filters (Fiber Bragg grating or Fabry-Pérot) [36], wavelength splitter/combiner, pulse compression (Figure 2.3) [37], monochromators [38], fiber couplers, sensors [39], acoustooptics, integrated optics, holography, optical data processing, and spectral analysis [40], among others.

The equation which rules over the grating response under oblique plane-wave incidence reads [35]:

$$n_{eff} \cdot sin\theta + n_o \cdot sin\phi_m = m \cdot \frac{\lambda}{\Lambda} \tag{2.1}$$

Where n_{eff} is the grating effective index, n_o is the background refractive index, θ and ϕ_m are the incident and refracted m^{th} order angle respectively, m is the called order number, λ is the wavelength and Λ is the grating periodicity.

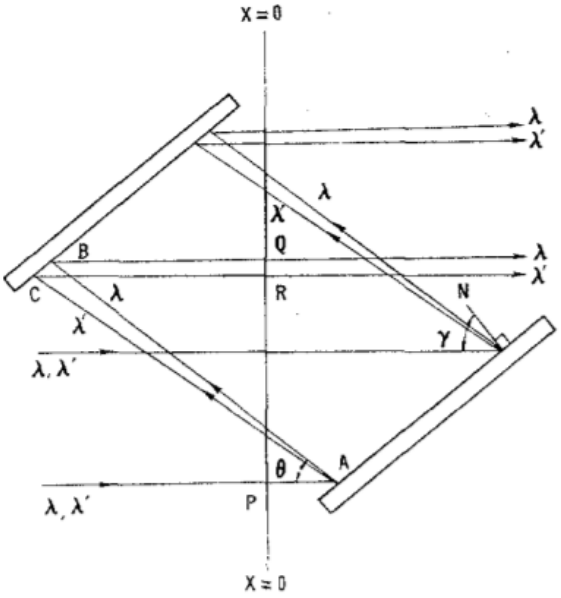

Figure 2.3: Diffraction grating used for pulse compression [37]

When employing the grating as an antenna where the input waveguide is directly connected to the grating (Figure 2.4), the incident beam is perpendicular to the grating normal vector. In other words, $sin(\theta) = 1$ and the grating equation is [41]:

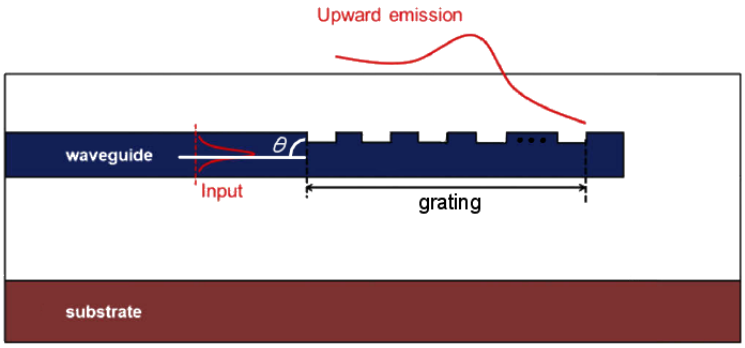

Figure 2.4: Waveguide-Grating connection [41]

$$n_0 \cdot sin\phi_m = n_{eff} - \frac{m \cdot \lambda}{\Lambda} \tag{2.2}$$

Lastly, the m^{th} order which satisfies the so-called Bragg condition usually (but not always) maximizes its diffraction efficiency [40]. This parameter will be considered as one of the most

important ones since it is related to the gain of the structure and indirectly with its directivity. The Bragg condition occurs if the wavelength and the angle of incidence wave satisfy the relationship [35]:

$$m = 2\Lambda \cdot n_{eff} \cdot cos(\theta - \phi_m) \tag{2.3}$$

Since $\theta = \pi/2$, Equation 2.3 can be simplified for a grating antenna scenario to:

$$m = 2\Lambda \cdot n_{eff} \cdot sin(\phi_m) \tag{2.4}$$

2.2 Design of a 3D wireless switch

The objective of this part is to develop the design for the 3D wireless switch based on the previous theoretical basis the measured GST properties, optimizing its performance, examining its characteristics and laying down the device characteristics. The final results will be the materials needed, the specification of the model's geometry and its properties.

2.2.1 Design and optimization

Firstly, for this application, we will study the different grooves commonly used in gratings (Figure 2.5). Production limitations must be taken into consideration when choosing the profile for the device. Since GST is deposited over the structure in layers, only the laminar or binary grating can be used (Figure 2.6).

Secondly, we will optimize the parameters theoretically extracted to maximize the characteristics of the device, specifically directivity, gain, efficiency, losses, reflections, side lobes and switching resolution. Insertion losses will be defined by parameter S_{21}, as it represents the proportion of the field in the output port when the input port is excited and reflections by parameter S_{11}, representing the field that is measured at the input port when it is fed. We define the side lobe level (*SLL*) as the difference between the maximum gain value found in the radiation diagram and the non-symmetrical second maximum found, as in gratings, there are techniques to redirect or suppress the symmetrical beam. The optimal values for a communication device are the following:

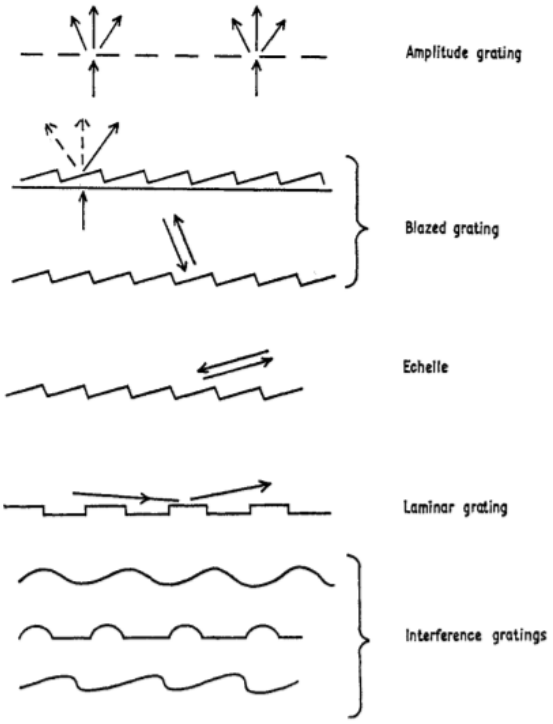

Figure 2.5: Types of gratings [42]

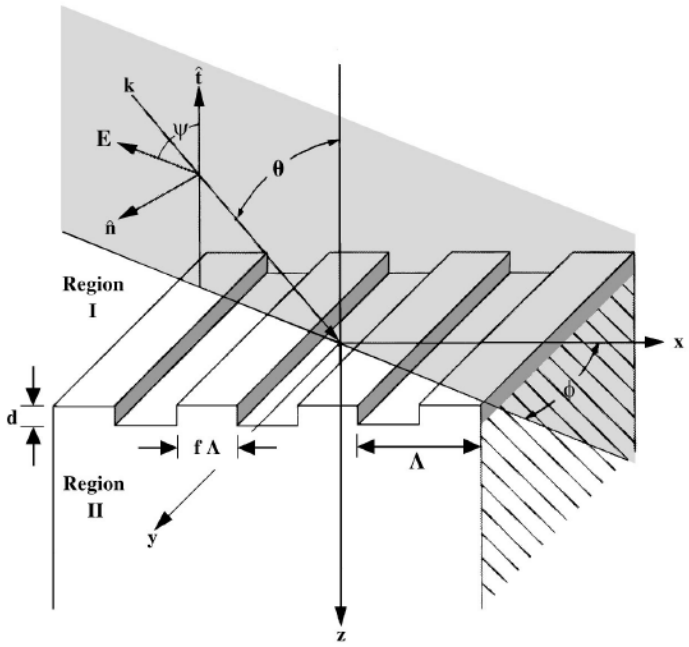

Figure 2.6: Grating scheme [43]

	Value [Lin]	Value [dB]
Directivity	>20	13
Gain	>10	10
S_{11}	0.1 to 0.01	-20 to -40
S_{21}	1	0
SLL	0.1	-10

Table 2.1: Communication standard

Considerations

For the development of the design, several approximations, considerations and specifications were taken into account. It was studied that with a fixed grating width, the effective index was invariant to small changes in the periodicity of the grating (Λ), filling factor (ff), etching (d) and number of periods (N).

Due to the large electrical size of the considered device, the different moduli of the structure were simulated independently: waveguide input, grating adapter, grating, antenna adapter and rectangular antenna. We consider two sets of components: the two main radiating structures (grating and rectangular antenna) for the antenna parameters and structural segments (waveguide input, grating adapter, antenna adapter) to calculate the losses added to the system. The whole device will be structured in cascade from waveguide input to rectangular antenna as shown in Figure 2.7.

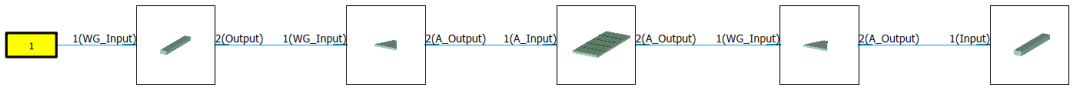

Figure 2.7: Antenna modular components

The simulation program port excitation propagates one mode into the simulated device. Bringing the fact that the design is built as an assemblage, the individual moduli are independently fed without taking into consideration the structures before. To cope with this handicap, there are two solutions: the simulation of the design as a whole or the characterization of the modes and excitations in each port.

In order to compare the modes simulated in CST we evaluate the output matrices in MATLAB measuring the value of every component on each point.

Let A and B be two fields, $\mathcal{S}$ will be defined as the magnitude of similarity between the fields A and B:

$$\mathcal{S} = \frac{\iint_S A \cdot B^* dS}{\sqrt{\iint_S A \cdot A^* dS \iint_S B \cdot B^* dS}} \tag{2.5}$$

Since the simulation outputs a matrix of NxMx2D values, being N and M the total discretization points in the x and y coordinates and D the dimensions considered, we can integrate by Simpsons' method:

$$\iint_S A \cdot B^* dS = \sum_{i,j}^{N,M} A_{i,j} \cdot B^*_{i,j} dS \tag{2.6}$$

Since the discretization uses equidistant points, the surface dS we will be multiplying is a constant, and we can simplify up to:

$$\mathcal{S} = \frac{\sum_{i,j}^{N,M} A_{i,j} \cdot B^*_{i,j}}{\sqrt{(\sum_{i,j}^{N,M} A_{i,j} \cdot A^*_{i,j}) \cdot (\sum_{i,j}^{N,M} B_{i,j} \cdot B^*_{i,j})}} \tag{2.7}$$

Due to the fact we are considering a wave interface between two media, its boundaries are fixed by the boundary condition for dielectrics:

$$n_{1,2} \times (E_2 - E_1) = 0 \tag{2.8}$$

$$n_{1,2} \times (H_2 - H_1) = 0 \tag{2.9}$$

Therefore, while calculating the similarity between modes, it is only considered the tangent fields to the interface, in our case: E_x, E_y, H_x and H_y.

With this tool, we will later on (Section 2.2.2) calculate the accuracy of the input modes to assure the simplification of the model by modules. It will depend on the materials and sizes of the input guide, as they define the modes that are stimulated by the simulation program.

2.2.2 Final design

We start by deciding the materials we use in the design. The characteristics of the materials are founded on its refractive index and its similarity and differentiability from the substrate and background material. For this purpose, we consider several GST compounds for their phase-change non-volatile memory state change and the wide range of types (stoichiometries), offering an ample catalogue of refractive index distributions (Figure 1.5).

As we work at the 3^{rd} window of telecommunications (λ = 1.55 μm , E = 0.8 eV or f = 193.414 THz), we have to find a substrate material that matches the real part of the GST permitivity (ε_1) in the amorphous phase.

Therefore, for the substrate and background material we consider two options: $Si(\varepsilon_{Si} = 11.9) - SiO_2(\varepsilon_{SiO_2} = 2.1)$ and $Ge(\varepsilon_{Ge} = 18.06) - GeO_2(\varepsilon_{GeO_2} = 2.52)$. It is shown in Figure 2.8a that the two only viable setups are $Ge - GeO_2 - GST_{214}$ and $Ge - GeO_2 - GST_{224}$, as ε_{Si} is too low for this set of materials. We finally use the first set-up ($Ge - GeO_2 - GST_{214}$) since its losses in the crystalline phase are lower (see Figure 1.5d) and its change of index is significantly higher (see Figure 2.8b). It must be said that at 1550nm we find the maximum phase-change of GST_{214} .

We also considered shifting to λ = 3.3 μm, in order to use a Silicon, as n_{Si} is higher at lower wavelengths ($n_{Si,3.3\mu m} = 3.42$), and the refractive index we extracted showed a n = 3.78 at that wavelength.

For the $Ge-GeO_2-GST_{214}$ component, we calculate the dimensions of the structure, starting with the width of the grating (width along the *y*-direction in Figure 2.6) as it conditions the grating effective refractive index, which is approximately constant for widths above 2.5 μm. The wider the structure, the more directive it is, since the wave output by the grating is wider and closer to a plane wave. However, the magnitude of the simulation grows exponentially by increasing the width. Then we set a 3 μm value as it provides a good balance between efficiency and simulation size. Therefore, the effective refractive index of the structure is $n_{eff} = 3.72558$ as the simulation outputs.

Subsequently, we check the mode matching of the modular structure, as we already have the different variables to model the input modes: materials ($Ge - GeO_2$), and input dimensions

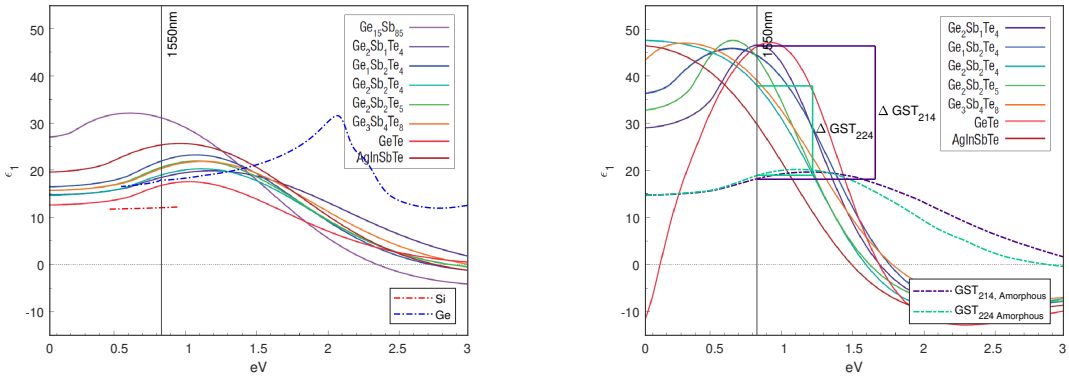

(a) ε_{Ge}, ε_{Si} **and** $\varepsilon_{GST_{214,Amorphous}}$ **(b)** $\varepsilon_{1GST_{C}rystalline}$

Figure 2.8: ε comparison

Figure 2.8a displays the value of ε_1 for the different amorphous GST compounds (colored solid lines), the ε_1 of Silicon (red dash-dotted line) and Germanium (blue dash-dotted line) and a vertical line at the working frequency (1550nm = 0.8eV). Figure 2.8b displays the value of ε_1 for the different crystalline GST compounds (colored solid lines), $\varepsilon_{1\text{Amorphous}}$ of GST_{214} and GST_{224} (purple and turquoise dash-dotted lines respectively) and the variation of index experienced in the phase-change.

(waveguide of 0.45x0.25 μm and grating of 2.5x0.25μm). To ensure the values generated are accurate, we choose a threshold of 95% of fields similarity on average. Considering the symmetry of the linkage of the structure, Figure 2.9 shows the two interfaces taken into consideration, Figure 2.10 the error of the approximation between the two bordering fields, and Table 2.2 the percentage of similarity in the interface. Each one of them is segmented into two components (E field and H field) in order to differentiate the error added by each component.

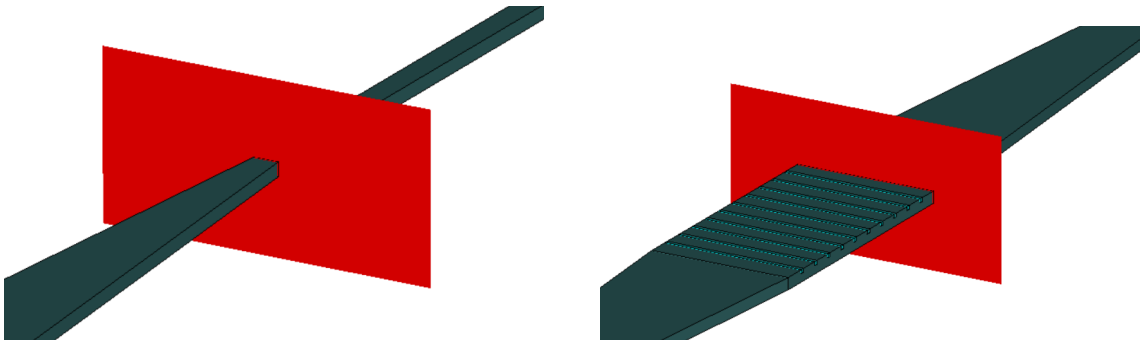

(a) Waveguide-Adapter interface structure **(b) Adapter-Grating interface structure**

Figure 2.9: Close-up interfaces

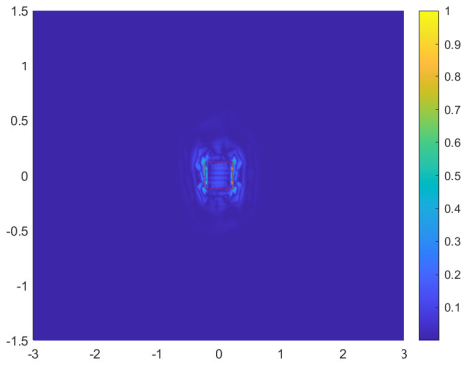

(a) Waveguide-Adapter: E interface error

99.65%

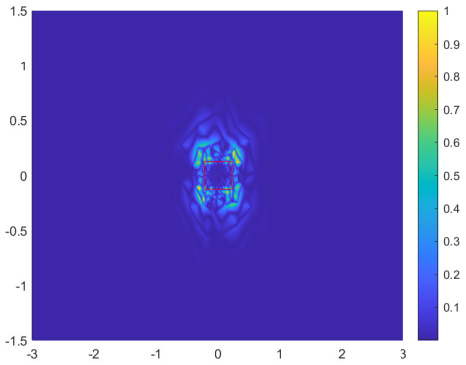

(b) Waveguide-Adapter: H interface error

95.49%

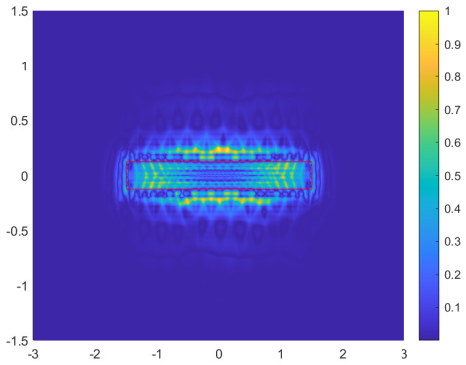

(c) Adapter-Grating (A): E interface error

99.96%

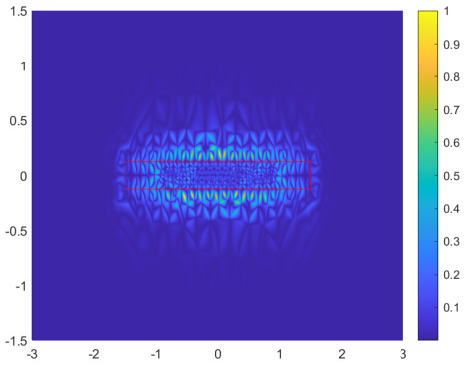

(d) Adapter-Grating (A): H interface error

98.09%

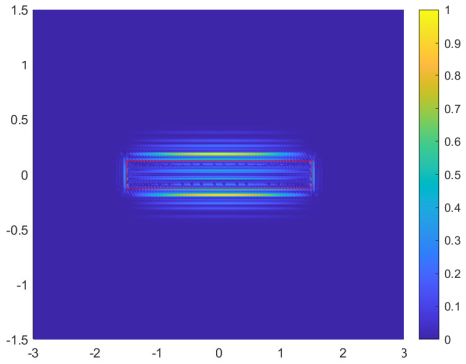

(e) Adapter-Grating (C): E interface error

99.99%

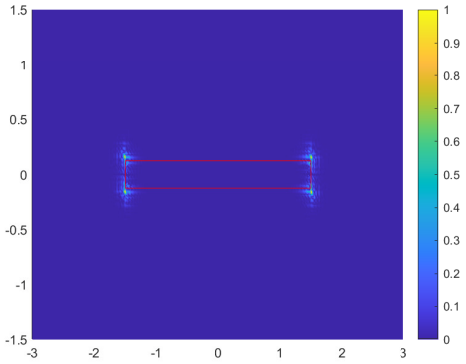

(f) Adapter-Grating (C): H interface error

99.25%

Figure 2.10: Fields similarity error (%)

	Waveguide - Adapter	Adapter - Grating A	Adapter - Grating C
E Similarity	99.65%	99.96%	99.99%
H Similarity	95.49%	98.09%	99.25%

Table 2.2: Extracted similarity

Considering the output data, the main differences shown in the interface are related to the boundaries and edges of the germanium, the regions with the most differences are confined in rather small differentials of surface obtaining high similarities. The error shown in Figure 2.10 also shows that the shape of the modes in the interfaces are alike, in other words, the first mode excited in each interface is similar and consistent.

The lower value of similarity is found in the interface Waveguide - Adapter (Figure 2.9a) at the H field. This value of 95.49% is above the threshold set as the objective. Hence, the modular segmentation is an acceptable approximation for this project and we can keep obtaining the other parameters of the structure.

Following the effective refractive index obtained before, we are able to calculate the optimal grating period (Λ). By isolating Λ in both equations 2.4 and 2.1, being $\phi_{optimum}$ the first order angle of radiation that maximizes the Bragg condition, n_{eff} the effective refractive index of the grating and n_0 the refractive index of the background material (for this structure GeO_2), we obtain:

$$\phi_{optimum} = sin^{-1}(\frac{n_{eff}}{2 \cdot n_{eff} + n_0}) \tag{2.10}$$

The optimum value of the structure is achieved when $\phi = 24.2332°$. Thus, from Equation 2.1:

$$\Lambda_{optimum} = \frac{m \cdot \lambda}{n_{eff} - n_0 \cdot sin\phi_{optimum}}; m = 1 \tag{2.11}$$

As a result, we find $\Lambda_{optimum} = 0.50466\mu m$

Laying the bases of the modular simulation and the basic dimensions, we move on to the device's performance. As previously said, the structure consists of two main radiating segments: the grating and the output antenna. We define two optimal working scenarios for the grating: transmission and radiation. These scenarios are defined by the state of the GST in the grating: amorphous and crystalline respectively.

As previously said, in the amorphous state, the ideal performance is the GST_{214} to be perceived as Germanium since $\varepsilon_{Ge} \simeq \varepsilon_{GST_{214}}$ (Figure 2.8a), consequently achieving the maximum transmission.Secondly, in the crystalline state, the ideal scenario is the GST_{214} to change its optical properties (Figure 2.8b) and reshape the geometry of the component, acquiring a grating-like behaviour.

To face the analysis of the characteristics needed from the device to work, we will examine the S parameters in both states. Due to the assemblage model, the parameter $S_{2,1}$ is added to the radiated field of the modules down the line as it represents the field that goes through a component and is transferred to the next one.

A coarse parametric sweep is used as a starting point for the optimization. The free parameters for the parametric sweep are the grating edge dimension ($(1-ff)\cdot\Lambda$ and d in Figure 2.6, defined in the simulation as ez and ey respectively).

We set the values of $(1-ff)\cdot\Lambda$ and d to $0.08\mu m$ (see Figure 2.11) as it represents a good enough trade-off of three out of four specifications, except the parameter $S_{1,1}$ as it represents its maximum (Figure 2.11c) and it is discussed later on.

The number of grating periods simulated is set to 10 since it seems to obtain significant results for the thesis without extending the simulation process of the structures. Further work should be done over this matter as the optimal point we set is not invariant with *N*. As N increases the optimal point of the grating dimensions $(1-ff)\cdot\Lambda$ and d are reduced.

Similarly, we consider the performance of the amorphous state and its objective specifications: high transmission and low reflection. As shown in Figure 2.12a, at 1550 nm the grating in amorphous state lets closely all the field to go through (see Table 2.3). In this case, the $S_{2,1}$ are considered input losses of the grating diminishing the performance of the taper antenna. This value is around -0.43dB for a 10 period grating.

On the other hand, in the crystalline state, a low $S_{2,1}$ is seek to suppress the radiating properties of the taper antenna. At 1550nm the $S_{2,1}$ of the crystalline grating reaches -23.13dB. This value is acceptable, and it defines maximum gain of the antenna used in the transmission scenario.

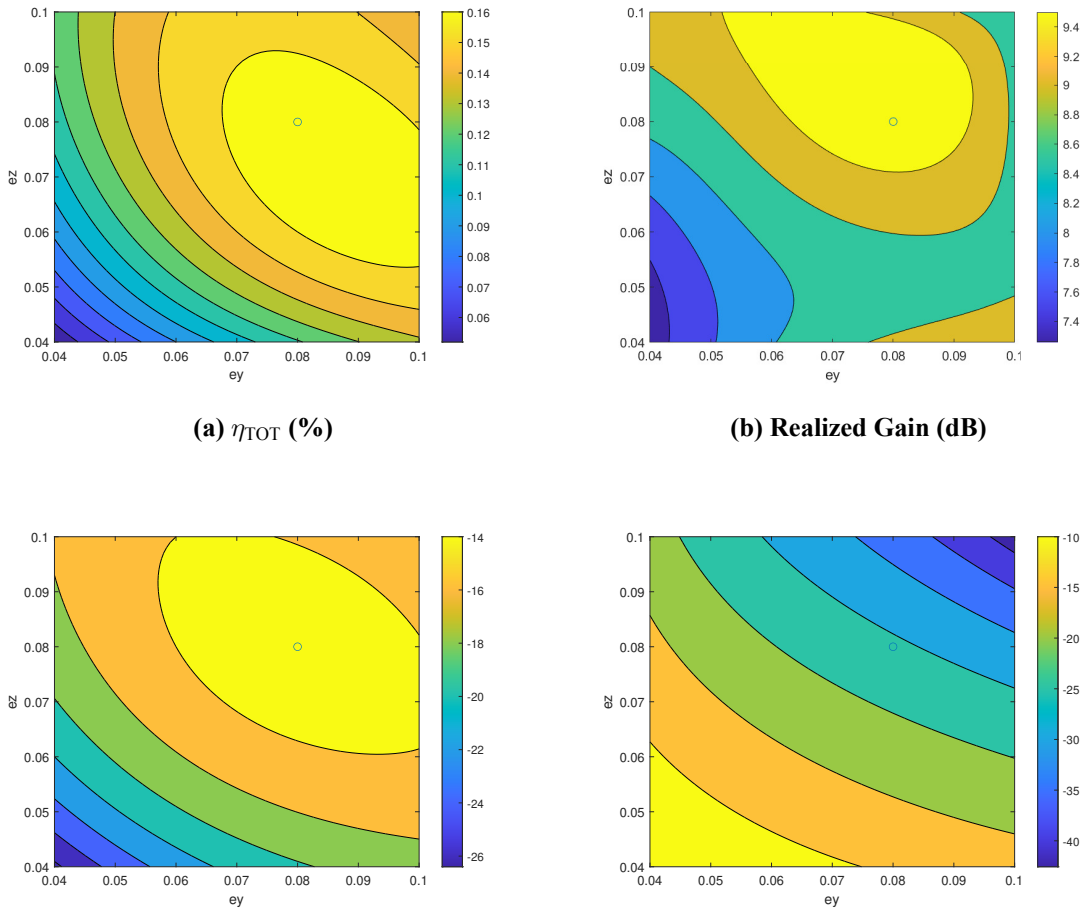

(a) η_{TOT} **(%)**

(b) Realized Gain (dB)

(c) $S_{1,1}$ **(dB)**

(d) $S_{2,1}$ **(dB)**

Figure 2.11: Coarse grating properties in crystalline state

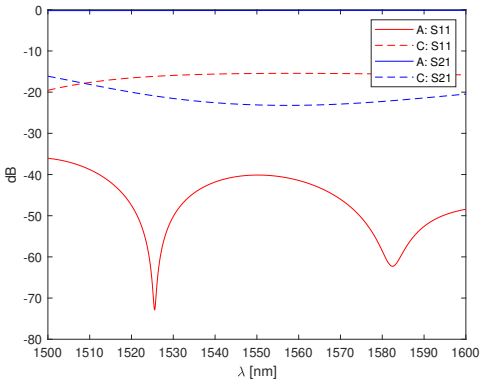

(a) Amorphous and Crystalline Grating

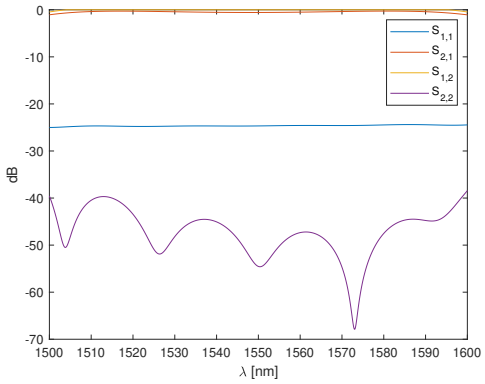

(b) Taper adapter

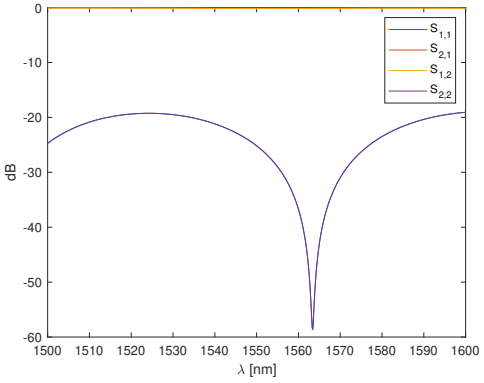

(c) Waveguide[1]

Figure 2.12: S Parameters

	$S_{1,1}$	$S_{2,1}$
Amorphous grating	-40.14dB	-0.43dB
Crystalline grating	-15.46dB	-23.13dB

Table 2.3: Grating S Parameters at 1550nm[2]

[1]The waveguide was expected to be perfect and without reflections, this could potentially be a numerical error of the simulation program

[2]S parameters are considered to be symmetrical $S_{1,1} = S_{2,2}$ and $S_{1,2} = S_{2,1}$ since the device is reciprocal and symmetrical

$S_{1,1}$	$S_{2,1}$	$S_{1,2}$	$S_{2,2}$
-24.67dB	-0.34dB	-0.57dB	-54.38dB

Table 2.4: Taper adapter S Parameters at 1550nm

As for the parameters $S_{1,1}$, the optimal scenario is to achieve a -20 to -30dB in all scenarios. However, in the crystalline phase this is not possible and an isolator must be used if the devices in the system are sensitive to the reflected waves or a optimization and perfection of the grating design to reduce the reflected field.

Minding the radiating properties, we lay the gain farfields at the working frequency, in order to check the main characteristics we are able to extract from a 2D farfield cut: the direction of steering, the gain in the main direction, the -3dB beam width and the SLL.

To begin with, we study the radiation of the grating and afterwards design the transmission antenna based on the parameters extracted from the grating in order to match the values and balance the transmission/grating radiation.

Firstly, we consider the individual gain of each phase (Figure 2.14a). The goal is to match both phases gains at the steering direction. The crystalline phase grating is used as the maximum gain achievable as it presents the most constraining parameters and efficiencies ($\eta_{\text{TOT}} \lesssim 0.2$). The total gain of the antenna is 9.23dB when considering all the insertion losses of the components used to connect the grating to the input waveguide. These losses also affect the antenna used as the horizontal radiating element in the amorphous phase. Therefore, its performance is required to be overachieved by 1.34dB (sum of all losses in cascade).

In order to achieve these specifications, we use an inverted taper antenna [28] with a tip distance of $2.5\mu m$ and a tip width of 100nm. With this configuration, a total gain of 8.85dB is obtained. It must be said that the gain of the horizontal antenna is easily increased by incriminating the tip length as stated in [28].

The final design effectiveness is defined by the extinction ratio at the steering direction. This parameter depicts the switch's phase shift variation in gain. As the second lobe in the amorphous state corresponds to the direction of steering of the crystalline state, the extinction ratio achieved is 9.69dB.

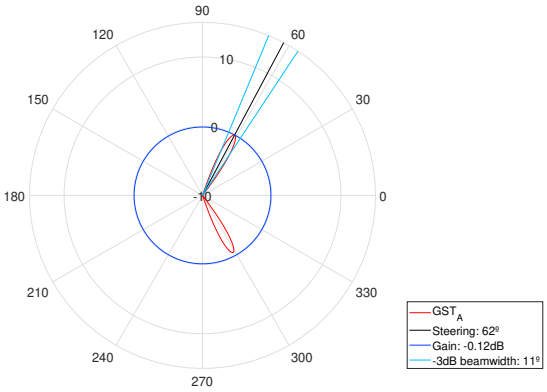

(a) Amorphous state: Grating

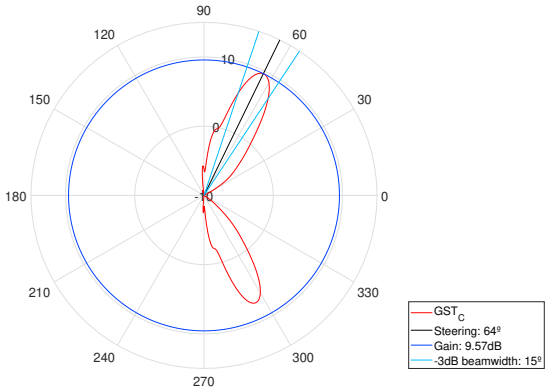

(b) Crystalline state: Grating

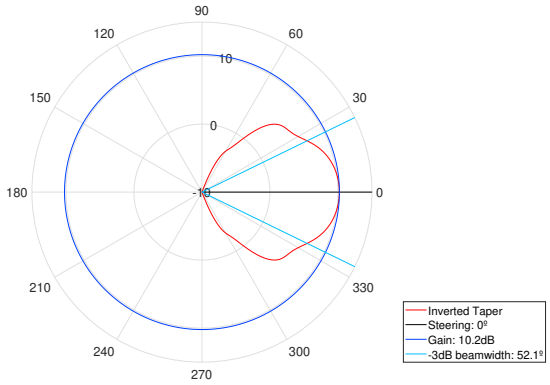

(c) Inverted Taper

Figure 2.13: Far fields gain: independent antennas

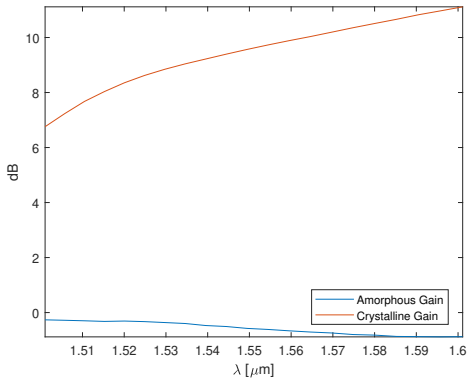

(a) Grating

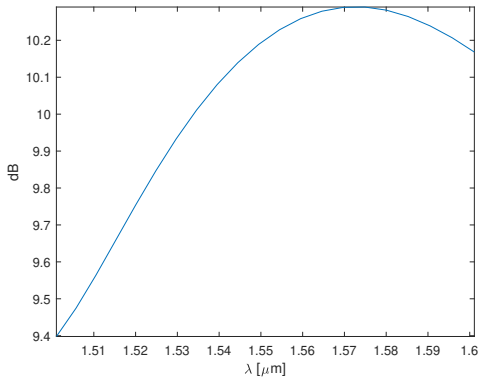

(b) Taper

Figure 2.14: Gain over frequency independent antennas

	Grating Amorphous	Grating Crystalline	Inverted Taper Amorphous
Steering Direction from x direction (F. 2.6)	62º	64º	0º
Gain	-0.12dB	9.57dB	10.2dB
-3dB Beam width	11º	15º	52.1º
SLL	-0.14dB	-15.37dB	-32.1dB

Table 2.5: Radiation properties

2.3 Results

The final structure realized gain is shown in Figure 2.15 by using the dimensions at Tables 2.6, 2.7 and 2.8. The final structures achieve the optimal specifications for the limitations of computer power. Grating sizes could be extended to tenths of micrometers. Therefore our structure is bound to increase its performance when scaled up.

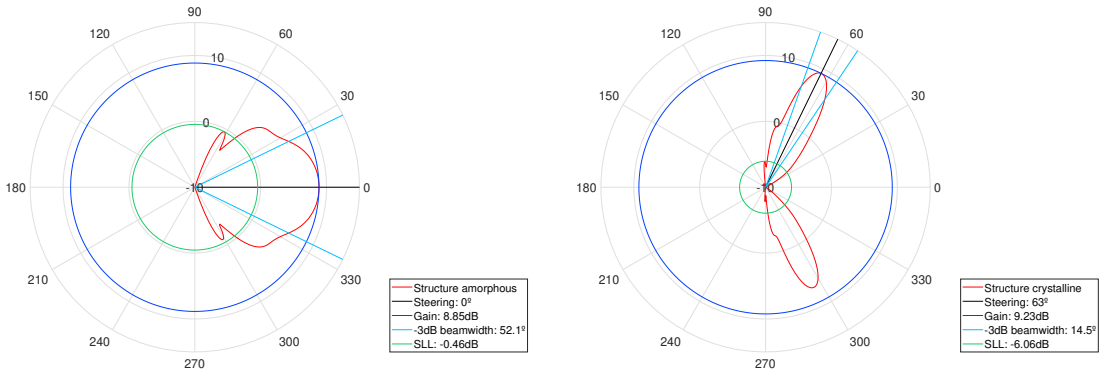

(a) Amorphous state **(b) Crystalline state**

Figure 2.15: Structure gain farfield

Length	Height	Tip width
2.5 μm	0.25 μm	0.1 μm

Table 2.6: Inverted taper dimensions

[3] Not to scale

Period (Λ)	Edging (d)	Filling factor (ff)	Number of periods	Height	Width
504.66 nm	80 nm	15.85%	10	250 nm	3 μm

Table 2.7: Grating dimensions

Port 1 width	Port 2 width	Height
450 nm	3 μm	250 nm

Table 2.8: Adapter dimensions

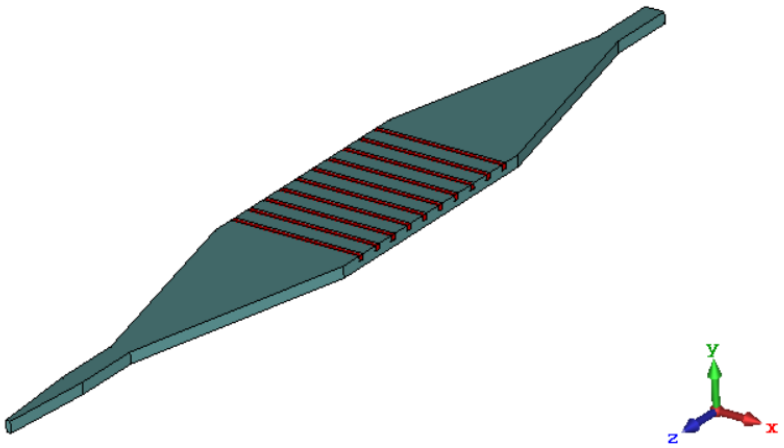

Figure 2.16: Final model view[3]

Part IV

Discussion

Chapter 1

Discussion

1.1 Conclusion

To conclude the thesis, the objectives and milestones presented in Chapter 1 were achieved. The framework of both PCM and switching were presented as the bases and we elaborated on them.

As a result of this thesis, we developed an algorithm to obtain the optical characteristics of a certain stoichiometry of GST with only the data from the reflection of the sample. It is shown that the optical characterization of this kind of materials is fundamental due to its inherent behaviour.

We also have designed a small footprint CMOS-compatible 3D non-volatile interconnector with switching properties with a gain of 9.23dB - 8.85dB (switching resolution of 9.69dB) at 1550nm with scalable parameters. The computational limitations of the work yield lower specs than expected for the telecommunication standard. However, this design has further work to explore as lowering the grating dimensions ($(1-ff)\cdot\Delta$ and d) increments the fraction of the energy the grating lets through. Because of this, it is possible to achieving a significant increment of the design's performance by increasing the number of periods of grating without incurring in a significant increment of losses.

The current model is Ge-based at λ = 1.55 μm but the setup can be shifted to Si-based technology if the $\varepsilon_{1Amorphous}$ of the PCM is reduced to a close enough value to ε_{1Si} or shifted to λ = 3.3 μm. The later option could also leverage on the fact that PCM commonly present their minimum losses at lower frequencies, ie. GST_{225} has its minimum at λ = 3.3 μm.

1.2 Future work

The refracted beams created by the grating must be discussed, considering the potential impacts of the diffracted energy. There are two approaches when optimizing the whole volume of multilayer structure: the transmittance of the energy through the substrate or the total reflection of the energy.

The first option relies on the zero reflectance quarter-wave–thick layer: ”quarter-wave–thick film of index $\sqrt{n_0 \cdot n_1}$ will reduce to zero the reflectance of a surface between two media of indices n_0 and n_1” [44]. Therefore, the thickness of the GeO_2 layer must be an odd multiple of $\frac{\lambda}{4 \cdot \sqrt{n_0 \cdot n_1}}$ allowing all the diffracted beam of negative orders to be transmitted into the substrate.

The second option reflects the bottom beams in the substrate and adds the waves in phase as a resonator cavity, redirecting the energy towards the upper cladding (as shown in Figure 1.1).

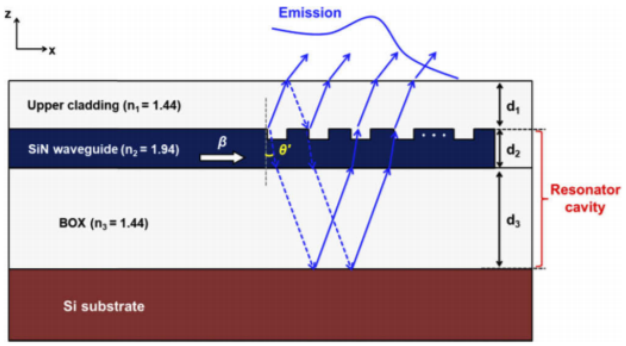

Figure 1.1: Grating resonator cavity [41]

Both solutions avoid unwanted reflected beams at the substrate perfecting the performance of the multilayered structure.

It must be said that the design production could be complex since GST needs to be deposited on narrow edges. This can be overcome by adding a layer on top of the structure. The purpose of this layer is to ease the deposition of the GST all over the grating. However, it is expected to increase the reflections experienced in the grating and lowering the efficiency due to the losses introduced by the GST in the crystalline state. On the other hand, it is also expected to reduce the 0^{th}-order reflection if the thickness layer used is [45]:

$$h = \frac{\lambda}{4n_2} \tag{1.1}$$

Being *h* the thickness of the added layer, λ the working frequency and n_2 the refractive index of the substrate. The $\lambda/4$ layer introduces a π phase shift at the reflections in the interfaces without compromising the optical specifications of the structure as it also relies on the zero reflectance quarter-wave-thick layer.

For the index retrieval algorithm, transmission measurements could be added, as the TMM method already calculates its values. This only requires a different substrate used instead of gold and increasing the number of layers taken into consideration by the TMM. With this incorporation, the error calculated acquires another degree of freedom since it could be a combination of both errors (transmission and the reflection) or the maximum of both. This could be useful as we have experienced different behaviours for the optimization when minimizing the error with the sum of errors or its maximum.

References

[1] Iraj Sadegh Amiri et al. “Introduction to photonics: Principles and the most recent applications of microstructures”. In: *Micromachines* 9 (9 Sept. 2018), p. 452. ISSN: 2072666X. DOI: 10.3390/mi9090452. URL: www.mdpi.com/journal/micromachines.

[2] J.D. Meindl. “Low power microelectronics: retrospect and prospect”. In: *Proceedings of the IEEE* 83.4 (1995), pp. 619–635. DOI: 10.1109/5.371970.

[3] Igor L Markov. “Limits on fundamental limits to computation”. In: (2014). DOI: 10.1038/nature13570. URL: http://cnx.org/content/m32874/.

[4] Radhakrishnan Nagarajan, Christopher Doerr, and Fred Kish. *Semiconductor Photonic Integrated Circuit Transmitters and Receivers*. Elsevier, 2013. DOI: 10.1016/B978-0-12-396958-3.00002-0.

[5] J. F. Liu et al. “Waveguide integrated Ge p-i-n photodetectors on a silicon-on-insulator platform”. In: 2006, pp. 1–4. ISBN: 1424408164. DOI: 10.1109/OVCISO.2006.302697.

[6] Ali K Okyay et al. “Silicon Germanium CMOS Optoelectronic Switching Device: Bringing Light to Latch”. In: *IEEE TRANSACTIONS ON ELECTRON DEVICES* 54 (12 2007). DOI: 10.1109/TED.2007.908903. URL: http://ieeexplore.ieee.org..

[7] J. Leuthold, C. Koos, and W. Freude. “Nonlinear silicon photonics”. In: *Nature Photonics* 4 (8 Aug. 2010), pp. 535–544. ISSN: 17494885. DOI: 10.1038/nphoton.2010.185. URL: https://www.nature.com/articles/nphoton.2010.185.

[8] Papichaya Chaisakul et al. “Integrated germanium optical interconnects on silicon substrates”. In: *Nature Photonics* 8 (6 May 2014), pp. 482–488. ISSN: 17494893. DOI: 10.1038/nphoton.2014.73. URL: https://www.nature.com/articles/nphoton.2014.73.

[9] Gary A. Sevison et al. “Free-Space optical switching of GST phase-change thin films via 1550 nm light”. In: OSA, 2018. ISBN: 978-1-943580-42-2. DOI: 10.1364/CLEO_AT.2018.JTu2A.6.

[10] Yifei Zhang et al. “Broadband transparent optical phase change materials for high-performance nonvolatile photonics”. In: *Nature Communications* 10 (1 Dec. 2019), pp. 1–9. ISSN: 20411723. DOI: 10.1038/s41467-019-12196-4. URL: https://doi.org/10.1038/s41467-019-12196-4.

[11] Wei Zhang, Riccardo Mazzarello, and Evan Ma. “Phase-change materials in electronics and photonics”. In: *MRS Bulletin* 44 (9 Sept. 2019), pp. 686–690. ISSN: 08837694. DOI: 10.1557/mrs.2019.201. URL: www.mrs.org/bulletin.

[12] Carlos Ríos et al. “Integrated all-photonic non-volatile multi-level memory”. In: *Nature Photonics* 9 (11 Nov. 2015). ISSN: 1749-4885. DOI: 10.1038/nphoton.2015.182.

[13] Kevin J. Miller, Richard F. Haglund, and Sharon M. Weiss. “Optical phase change materials in integrated silicon photonic devices: review”. In: *Optical Materials Express* 8 (8 Aug. 2018). ISSN: 2159-3930. DOI: 10.1364/OME.8.002415.

[14] Kostiantyn Shportko et al. “Resonant bonding in crystalline phase-change materials”. In: *Nature Materials* 7 (8 Aug. 2008). ISSN: 1476-1122. DOI: 10.1038/nmat2226.

[15] *Nanoparticle characterization techniques*. Elsevier, Jan. 2019, pp. 303–319.

[16] Jeffrey C. Lagarias et al. “Convergence Properties of the Nelder–Mead Simplex Method in Low Dimensions”. In: *SIAM Journal on Optimization* 9 (1 Jan. 1998). ISSN: 1052-6234. DOI: 10.1137/S1052623496303470.

[17] M. Claudia Troparevsky et al. “Transfer-matrix formalism for the calculation of optical response in multilayer systems: from coherent to incoherent interference”. In: *Optics Express* 18 (24 Nov. 2010), pp. 24715–24721. ISSN: 1094-4087. DOI: 10.1364/OE.18.024715.

[18] A. V. Myshlyavtsev and V. P. Zhdanov. “The effect of nearest-neighbour and next-nearest-neighbour lateral interactions on thermal desorption spectra”. In: *Chemical Physics Letters* 162 (1-2 Oct. 1989), pp. 43–46. ISSN: 00092614. DOI: 10.1016/0009-2614(89)85063-8.

[19] A.V. Myshlyavtsev. *Surface Diffusion Modelling: Transfer Matrix Approach*. 2001. DOI: 10.1016/S0167-2991(01)80027-6.

[20] *Transfer-matrix method (optics)*. URL: https://en.wikipedia.org/wiki/Transfer-matrix_method_(optics) (visited on 04/21/2021).

[21] Mamadou Moustapha Diop et al. "Optimization and Modeling of Antireflective Layers for Silicon Solar Cells: In Search of Optimal Materials". In: *Materials Sciences and Applications* 9 (8 July 2018), pp. 705–722. ISSN: 2153-1188. DOI: 10.4236/msa.2018.98051. URL: http://www.scirp.org/journal/msa.

[22] M. Beye et al. "Optimization of SiNx Single and Double Layer ARC for Silicon Thin Film Solar Cells on Glass". In: *Research Journal of Applied Sciences, Engineering and Technology* 6 (3 June 2013). ISSN: 20407459. DOI: 10.19026/rjaset.6.4094.

[23] *Tauc-Lorentz Dispersion Formula*. Tech. rep. HORIBA.

[24] Aleksandar D. Rakić et al. "Optical properties of metallic films for vertical-cavity optoelectronic devices". In: *Applied Optics* 37 (22 Aug. 1998). ISSN: 0003-6935. DOI: 10.1364/AO.37.005271.

[25] *Data Centers and Servers*. URL: https://www.energy.gov/eere/buildings/data-centers-and-servers (visited on 12/05/2021).

[26] Xin Tu et al. *State of the art and perspectives on silicon photonic switches*. Jan. 2019. DOI: 10.3390/mi10010051. URL: www.mdpi.com/journal/micromachines.

[27] J. Michael Harris et al. "Liquid-crystal based optical switching". In: Springer US, 2006, pp. 141–167. ISBN: 0387261419. DOI: 10.1007/0-387-29159-8_5. URL: https://link.springer.com/chapter/10.1007/0-387-29159-8_5.

[28] Sergio Lechago Buendía. "All-dielectric nanoantennas enabling on-chip wireless silicon photonics". PhD thesis. Valencia (Spain): Universitat Politècnica de València, Nov. 2019. DOI: 10.4995/Thesis/10251/133074. URL: https://riunet.upv.es/handle/10251/133074.

[29] Mee-Koy Chin, Chee-Wei Lee, and Jinyuan Shen. "Polarization-independent vertical coupler for photonics integration". In: *Optics Express* 12 (1 Jan. 2004), p. 117. ISSN: 1094-4087. DOI: 10.1364/opex.12.000117. URL: http://www.opticsexpress.org/abstract.cfm?URI=OPEX-11-15-1724.

[30] P. K.J. Singaravelu et al. “Low-loss, compact, spot-size-converter based vertical couplers for photonic integrated circuits”. In: *Journal of Physics D: Applied Physics* 52 (21 Mar. 2019), p. 214001. ISSN: 13616463. DOI: 10.1088/1361-6463/ab07d5. URL: https://doi.org/10.1088/1361-6463/ab07d5.

[31] *IEEE Xplore Full-Text PDF:* URL: https://ieeexplore.ieee.org/stamp/stamp.jsp?tp=&arnumber=6758443 (visited on 02/04/2021).

[32] *Monopole antenna - Wikipedia*. URL: https://en.wikipedia.org/wiki/Monopole_antenna (visited on 02/02/2021).

[33] Carl G Chen and Mark L Schattenburg. *A Brief History of Gratings and the Making of the MIT Nanoruler*. Tech. rep. 2004.

[34] George R. Harrison. “The Production of Diffraction GratingsI Development of the Ruling Art*”. In: *Journal of the Optical Society of America* 39 (6 June 1949). ISSN: 0030-3941. DOI: 10.1364/JOSA.39.000413.

[35] Eugene Hecht. *Optics*. 4th. Addison-Wesley, 2002. ISBN: 0321188780.

[36] Raymond M. Measures. “Fiber-Optic-Based Smart Structures”. In: Elsevier, Jan. 2003, pp. 769–802. DOI: 10.1016/b0-12-227410-5/00241-6.

[37] Edmond B. Treacy. “Optical Pulse Compression with Diffraction Gratings”. In: *IEEE Journal of Quantum Electronics* 5 (9 1969), pp. 454–458. ISSN: 15581713. DOI: 10.1109/JQE.1969.1076303.

[38] Yi-Chen Chuang. *Monochromator*. Springer Berlin Heidelberg, 2015. DOI: 10.1007/978-3-642-27851-8_354-1.

[39] Raymond M. Measures. “Fiber-Optic-Based Smart Structures”. In: Elsevier, Jan. 2003, pp. 769–802. DOI: 10.1016/b0-12-227410-5/00241-6.

[40] T.K. Gaylord and M.G. Moharam. “Analysis and applications of optical diffraction by gratings”. In: *Proceedings of the IEEE* 73 (5 1985). ISSN: 0018-9219. DOI: 10.1109/PROC.1985.13220.

[41] Chul-Soon Im et al. “Silicon nitride optical phased array based on a grating antenna enabling wavelength-tuned beam steering”. In: *Optics Express* 28 (3 Feb. 2020), pp. 3270–3279. ISSN: 1094-4087. DOI: 10.1364/OE.383304.

[42] E W Palmer et al. *Diffraction gratings*. Tech. rep. 1975, pp. 975–1048.

[43] "Formulation for stable and efficient implementation of the rigorous coupled-wave analysis of binary gratings". In: *Journal of the Optical Society of America A* 12 (5 May 1995), p. 1068. ISSN: 1084-7529. DOI: 10.1364/josaa.12.001068.

[44] H. Angus Macleod. *Thin-Film Optical Filters*. Ed. by E Roy Pike and Robert G W Brown. 4th. CRC Press, 2017. ISBN: 978-1-4200-7302-7.

[45] Meifang Lai et al. "Multilayer porous silicon diffraction gratings operating in the infrared". In: *Nanoscale Research Letters* 7 (1 2012). ISSN: 1556-276X. DOI: 10.1186/1556-276X-7-645.